Applications of electron holography

Akira Tonomura

Advanced Research Laboratory, Hitachi, Ltd., Kokubunji, Tokyo 185, Japan

The development of a coherent field-emission electron beam has facilitated practical applications of electron holography. This paper reviews this field of growing importance, making special reference to the application of electron holography to current technological problems. It is seen that the phase distribution of an electron wave function transmitted through a specimen can be observed as an interference micrograph, thus providing considerable information about the microscopic distribution of electromagnetic potentials. For example, a magnetic sample's contour fringes directly indicate its magnetic lines of force. These fringes can also show the equipotential lines of an electric sample and thickness contours of a homogeneous specimen. Holographic techniques can be effectively employed to improve the accuracy of phase measurements up to an order of $2\pi/100$. This opens the way for use of electron holography as a high-precision measurement method that can cast light on wide regions of the microscopic world pertinent to both basic science and practical industry.

CONTENTS

Introduction 639
I. Outline of Principles 640
A. Holography 640
B. In-line holography 640
C. Off-axis holography 641
D. Electron holography 642
II. Electron-Optical Components Employed for Holography 643
A. Coherent electron sources 643
1. Electron beam coherence 643
2. Thermionic cathode 645
3. Field-emission cathode 645
B. Interferometer 646
C. Electron lens 646
III. Historical Development of Electron Holography 648
A. Early experiments 648
B. In-line holography 649
1. Experimental trials 649
2. Image resolution 650
C. Off-axis holography 650
IV. Holographic Techniques for Displaying Phase Distribution 652
A. Hologram formation 652
B. Optical reconstruction for interference microscopy 652
C. Techniques for phase-difference amplification 653
V. Interpretation of Interference Electron Micrographs 654
A. Electron beam phases 654
B. Interpretation of contour maps 654
1. Classical treatment 654
2. Quantum-mechanical treatment 655
3. Some complex cases 656
VI. Practical Applications to Technological Problems 656
A. Measurement of electric potential distributions 656
B. Thickness measurements 657
1. Interpretation of contour maps 657
2. Fine-particles example 658
3. Phase-difference amplification 658
4. Future expectations 659
C. Observation of magnetic domain structures 659
1. Interpretation of contour maps 659
2. Example of ferromagnetic fine particles 660
3. Example of cross-tie wall 661
D. Measurement of magnetic field distributions 662
1. Application to high-density magnetic recording 662
2. Magnetic monopoles 663
E. Measurement of hidden magnetic flux through vector potentials 663
1. Significance of potentials—the Aharonov-Bohm effect 663
2. Observation of the flux quantization process— Experimental proof of the Aharonov-Bohm effect 665
Conclusions and Future Prospects 667
Acknowledgments 667
References 667

INTRODUCTION

The packing density of electronic devices is now increasing rapidly. Minimum size within such devices is moving into the submicron range; under such circumstances detail is no longer observable via conventional optical means. Instead, electron beams are beginning to play an important role. This increase in the importance of electron microscopy is resulting from the fact that it provides direct information about microscopic structures.

The functionality of electron-optical devices is still, however, extremely limited compared with optical systems. For example, techniques utilizing phase information, such as phase contrast or interference microscopy, have not been put to practical use in the field of electron microscopy until quite recently.

One approach that shows promise of overcoming this problem is electron holography, the subject of this paper. Through electron holography, electron wave fronts are transformed into light wave fronts on an optical bench. Consequently the limitations of electron microscopes can be overcome through use of versatile optical techniques.

Electron holography was devised by Gabor in 1949 as a way to extend the limits of electron microscope resolution (Gabor, 1949, 1951). However, its practical realization had to wait for the recent development of a coherent field-emission electron beam, as has also been the case for optical holography, for which the invention of lasers finally allowed the field to come into full bloom.

This paper provides an overview of the present status

of electron holography,[1] with special reference to its recent applications to problems on technological frontiers. Future prospects for the technology will also be touched upon.

I. OUTLINE OF PRINCIPLES

A. Holography

An optical lens forms the exact image of an object by focusing all rays from a point onto an image point through a lens. Holography, on the other hand, is a lensless imaging method, which relies only upon the interference phenomena of waves. Consequently holography is applicable to all kinds of waves—whether light, x-ray, sound, electron, or neutron waves—irrespective of the existence of a lens for each wave. A major feature of holography is that a complete wave, i.e., a complex amplitude, can be reconstructed from an exposed film, called a "hologram" (literally, a photograph containing all information). For this reason, holography can produce a stereoscopic picture before our eyes in a far more realistic manner than can any other technique.

The first step in holography consists of recording an interference pattern (hologram) between a scattered wave from an object and a reference wave. The amplitudes of the scattered and reference waves at the hologram plane are, respectively, designated φ_0 and φ_r. Since these are partial waves emitted from a single source, they are coherently superposed to interfere with each other. Intensity I at the hologram plane is given by $|\varphi_0+\varphi_r|^2$.

When the interference pattern is exposed onto film, the amplitude transmittance t is given by

$$t=I^{-\gamma/2}=|\varphi_0+\varphi_r|^{-\gamma}. \tag{1}$$

Here, γ indicates the contrast value of the film. If the condition $\gamma=-2$ is satisfied, though this is not necessarily indispensable for reconstruction, t can be expressed simply by I. The negative value of γ signifies reversal of the film.

The second step in holography consists of reconstructing the image of the original object. For simplicity, the hologram is illuminated with the same reference wave as that used in the hologram formation process. Transmitted amplitude T is then given by

$$\begin{aligned} T&=|\varphi_0+\varphi_r|^2\varphi_r \\ &=(|\varphi_0|^2+|\varphi_r|^2)\varphi_r+|\varphi_r|^2\varphi_0+\varphi_0^*\varphi_r^2 . \end{aligned} \tag{2}$$

The imaging properties of holography can be clearly understood simply by interpreting the terms in this equation. The first and second terms correspond to the transmitted wave. The third term is proportional to the scattered wave from the object. This means that the exact image can be reconstructed if this term can be observed separately from the others. The fourth term is similar to the third except that its phase value is opposite in sign relative to that of the reference wave. This term produces the conjugate image, the amplitude of which is the complex conjugate of the reconstructed image.

Holographic image formation seems to work perfectly up to this point. However, this is not the case when higher-order terms are taken into considerations. Aberrations accompanying this type of imaging are quite similar to those for an optical lens (Meier, 1965).

B. In-line holography

A simple example of holography is shown in Fig. 1(a) where a point object is illuminated with a plane wave. The transmitted plane wave can be regarded as a reference wave. This type of holography is called "in-line holography." Here, amplitudes of reference and object waves can be expressed by

$$\varphi_r=e^{ikz} \text{ and } \varphi_0=i\frac{f}{r}e^{ikr},$$

where f is the scattering amplitude from the point object. If f is real, the intensity distribution $I(x,y)$ at the hologram plane can be given by

$$\begin{aligned} I(x,y)&=|\varphi_0+\varphi_r|^2 \\ &=1+\left[\frac{f}{l}\right]^2-\frac{2f}{l}\sin\frac{k(x^2+y^2)}{2l}, \end{aligned} \tag{3}$$

where l is a distance between object and hologram. This interference pattern consists of concentric fringes, as illustrated in Fig. 1(b), and is called a "zone plate."

If this hologram is recorded on film with a contrast of $\gamma=-2$, and is then illuminated with a plane wave identical to the reference wave, it is possible to express the resultant transmitted amplitude $T(x,y)$ as

$$\begin{aligned} T(x,y)=e^{ikl}\Bigg[1+\left[\frac{f}{l}\right]^2+\frac{if}{l}\exp\left[\frac{ik(x^2+y^2)}{2l}\right] \\ -\frac{if}{l}\exp\left[-\frac{ik(x^2+y^2)}{2l}\right]\Bigg]. \end{aligned} \tag{4}$$

Here, the first and second terms represent the transmitted plane waves. The third term is identical to the original scattered wave from the point object, i.e., a spherical wave from point O [see Fig. 1(c)]. The fourth term represents a spherical wave from point O', which is at the mirror-symmetric position of O with respect to the hologram plane. This is the simplest conjugate image.

[1]Review articles on electron holography include those of Zeitler (1979), Rogers (1980), Wade (1980), Hanszen (1982), and Lichte (1982). A comprehensive review paper on electron interferometry has been provided by Missiroli, Pozzi, and Valdrè (1981).

In short, a hologram of a point object (i.e., a zone plate) functions as if it has both concave and convex lenses with the same focal length of l. Therefore illumination of a plane wave onto this hologram produces both divergent and convergent spherical waves.

This conclusion may also be arrived at in the following way. The incident wave is transmitted through only the concentric transparent parts of the zone plate. All paths from these parts to point O' have path differences of a multiple of a wavelength. Therefore all diffracted waves from the zone plate join in phase to form a focus by interfering at point O'. Furthermore, it can easily be found that diffracted waves from a virtual point source at O are also in phase.

Generally speaking, a reconstructed point image at O' cannot be observed separately. The defocused pattern of the conjugate point image at O is inevitably overlapped onto the reconstructed point image at O'. This results from the fact that the twin images both lie on axis. This problem of separating the twin image was, early on, a persistent obstacle to the realization of holography. A solution was found, however, with the introduction of a new method called "off-axis holography" (Leith and Upatnieks, 1962). With this method, a reference wave is tilted with respect to an object wave. Further details will be provided in the following subsection.

Although the conjugate image problem could be completely removed by introducing off-axis holography, efforts continued to reconstruct in-line holographic images that would be free from disturbances. Among them, the most effective method was seen to be Fraunhofer in-line holography. With this approach, in-line holograms are formed in a Fraunhofer diffraction plane of an object, i.e., under the conditions

$$a^2 \ll \lambda l \ . \tag{5}$$

Here a is the size of an object. If this condition is satisfied, the conjugate-image effect results only in a constant background near a reconstructed image (Develis, Parrent, and Thompson, 1966), as schematically shown in Fig. 2.

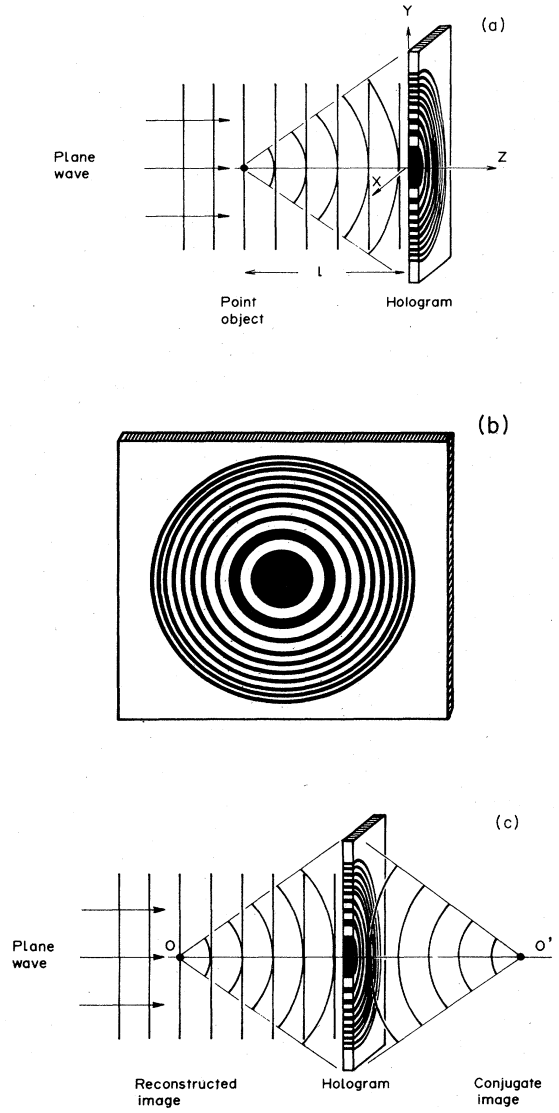

FIG. 1. Principle behind in-line holography: (a) hologram formation; (b) hologram of point object; (c) image reconstruction.

C. Off-axis holography

Off-axis holograms look quite different from in-line holograms. If a reference wave is assumed to be a tilted plane wave represented by $\varphi_r = e^{ik(z-\alpha y)}$, then intensity I at the hologram plane is given by

$$I(x,y) = 1 + |\varphi_0|^2 + \varphi_0 e^{-ik(l-\alpha y)} + \varphi_0^* e^{ik(l-\alpha y)} \ . \tag{6}$$

If a point object is again selected as an object, i.e., if $\varphi_0 = (if/r)e^{ikr}$ [Fig. 3(a)], the intensity leads to

$$I(x,y) = 1 + \left[\frac{f}{l}\right]^2 - \frac{2f}{l}\sin\left[\frac{k(x^2+y^2)}{2l} + k\alpha y\right] . \tag{7}$$

While the in-line hologram of a point object is a zone

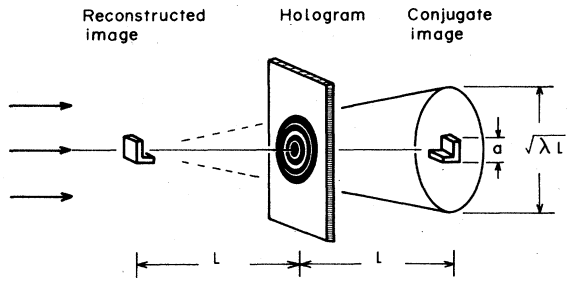

FIG. 2. Effect of conjugate image on reconstructed image. When a hologram is formed in a Fraunhofer diffraction plane of an object ($l \gg a^2/\lambda$), then the image can be reconstructed without disturbances from its conjugate image. This is because the reconstructed image is completely blurred to form a constant background near the conjugate image, or vice versa.

plate consisting of concentric circular fringes, this off-axis hologram is a sinusoidal grating modulated by an object wave [Fig. 3(b)].

If a plane wave $e^{ik(z-\alpha y)}$ illuminates the off-axis hologram represented by Eq. (6), the original object φ_0 is reconstructed. The propagation direction of the conjugate image is tilted by an angle 2α with respect to that of the reconstructed image [Fig. 3(c)]. Consequently the twin images are spatially separated, and they can be observed independently without any disturbance.

The imaging principle behind off-axis holography is not essentially different from that for in-line holography. One can see this from the fact that the off-axis hologram of a point object is also a zone plate, as is easily deducible from comparison of the two hologram intensities given by Eqs. (3) and (7). The only difference is the field of view of the zone plate. An in-line hologram can be compared to the axis region of an optical lens, while an off-axis hologram is similar to a peripheral part of the same lens. The imaging properties of the two are completely the same; only the position of the optical axis is different (see Fig. 4).

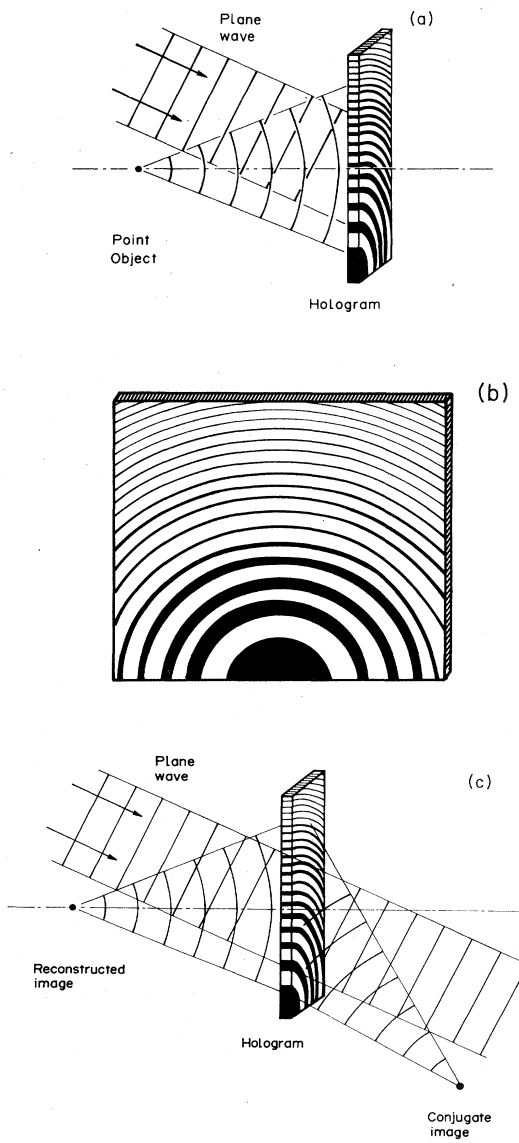

FIG. 3. Principle behind off-axis holography: (a) hologram formation; (b) hologram of point object; (c) image reconstruction.

D. Electron holography

With electron holography, the hologram formation wave is an electron wave, while the wave for image reconstruction is a light wave. One might wonder whether this is really possible, since the wavelengths of the two waves are so different from each other. For example, the wavelength of He-Ne laser light, 6328 Å, is larger than that of a 100-kV electron wave, 0.037 Å, by 200 000 times. In addition, the nature of the two wave fields is quite different: a light wave represents a classical force, whereas an electron wave represents a probability amplitude. There is also a difference in statistical notation, since Fermi-Dirac statistics are employed for electrons and Bose-Einstein for photons.

The problem of different wavelengths can be solved by enlarging electron holograms so that a light wave may be diffracted at an appropriate angle from the interference fringes in the holograms. This enlargement can be carried out by forming holograms through projection from a point electron source, or by using magnifying electron lenses. The former approach is the original method proposed by Gabor (1949). The latter, however, will be discussed in what follows, since it is more practical and provides a wider range of optical configurations.

It is easy to understand the imaging properties of electron holography if a zone plate is again taken as an example. An electron hologram of a point object, i.e., a zone plate, is magnified m times by electron lenses and recorded on film. An electron intensity distribution can be

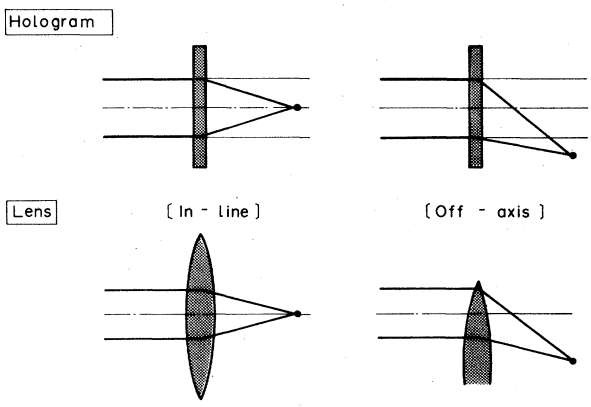

FIG. 4. Comparison of holography to lens action. In-line and off-axis holograms can be compared to central and peripheral parts of a lens, respectively.

recorded on film in the same manner as for light. The electron intensity is calculated, similarly to Eq. (3), to be

$$I(x,y)=1+\left[\frac{f}{l}\right]^2-\frac{2f}{l}\sin\frac{k[(x/m)^2+(y/m)^2]}{2l}\ , \tag{8}$$

where $k=2\pi/\lambda$ is the wave number of an electron beam.

When the hologram is illuminated with a light wave of wavelength λ', the transmitted amplitude at the plane l' distant from the hologram is given by

$$T(x,y)=e^{ik'l'}\left[1+\left[\frac{f}{l}\right]^2+\frac{if}{l}\exp\left[\frac{ik[(x/m)^2+(y/m)^2]}{2l}\right]-\frac{if}{l}\exp\left[-\frac{ik[(x/m)^2+(y/m)^2]}{2l}\right]\right]. \tag{9}$$

This equation has the same form as Eq. (4) if l' satisfies the relation

$$l'=m^2\frac{\lambda}{\lambda'}l\ . \tag{10}$$

This means that when a light wave illuminates the magnified electron hologram, an original wave front is reconstructed with longitudinal and lateral magnifications $m^2(\lambda/\lambda')$ and m, respectively. The fact that the lateral magnification is m is evident if the reconstruction of two point objects is taken into consideration (see Fig. 5); the distance between the two zone-plate centers in the hologram is equal to that between two reconstructed point images.

Both magnifications are equal to each other only if

$$m=\frac{\lambda'}{\lambda}\ . \tag{11}$$

In this case, the reconstructed wave front is scaled up by the wavelength ratio λ'/λ.

The simple discussions up to now hopefully point to the conclusion that holography is possible between two arbitrary waves, even though wavelengths and wave properties are different. This is because holography utilizes only the most fundamental features of a wave, i.e., interference and diffraction, which are common to all waves. To distinguish electron and optical waves by interferometry, one must examine their intensity correlations (Silverman, 1986).

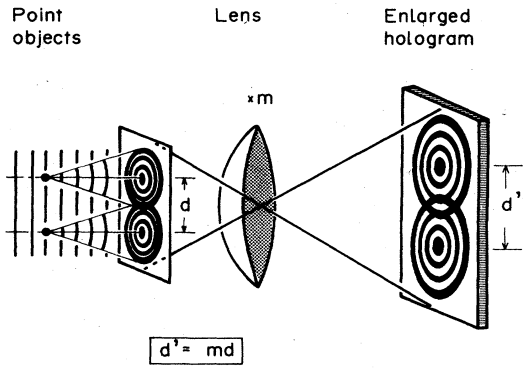

FIG. 5. Magnified in-line electron hologram. The lateral magnification of a reconstructed image is equal to hologram magnification m, irrespective of the wave length ratio, λ/λ'. On the other hand, the longitudinal magnification is different from m, but is given by $m^2(\lambda/\lambda')$.

II. ELECTRON-OPTICAL COMPONENTS EMPLOYED FOR HOLOGRAPHY

Before describing the expermental electron holographic procedures, it would be best to review some hardware components that are indispensable to the experiments, namely, the coherent electron source, electron beam splitter, and electron lens.[2]

A. Coherent electron sources

Up to this point holography has been discussed in terms of completely coherent waves. However, actual electron waves are far from completely coherent; electron holograms can only be formed under certain restricted conditions. Therefore coherence conditions for electron waves need to be looked at first. The number of interference fringes that can practically be observed with the existing electron beams will then be discussed.

1. Electron beam coherence

An electron beam like that in an electron microscope can be regarded as a system of successive incoherent wave packets emerging from a cathode. While the frequency of the wave packets is originally low, the additional conditions for observing interference fringes make this frequency drop still lower. The wave packets are too sparsely separated to overlap one another. The quantum interference that occurs in forming an electron hologram involves

[2]Specialists in electron interferometry or electron microscopy may be familiar with some or all of these items. Discussions in later sections will not go into their details; thus well-versed readers may jump ahead to the next section if they so desire.

one electron at a time, registering at a detector with an intensity proportional to the probability distribution; the interference fringes are built up one particle at a time.

To clarify the electron beam conditions under which an interference pattern can be observed, a simple example will be presented (see Fig. 6). Here, an incident wave packet passes through two small apertures forming an interference pattern. For the interference pattern to be observed, the phase relation of two partial waves has to be definite, first at the two apertures A and B, and second at a screen point. This imposes in simplified terms the following restrictions on the extension of a wave packet.

(1) The width of the incident wave packet must be large enough to cover the region between two points A and B.

(2) The length of the wave packet must be longer than the difference between two paths starting from points A and B and reaching a point at the screen.

The width of a wave packet is, in exact terms, the transverse coherence length, or l_t. This is determined by uncertainty in the propagation direction, or by the illumination angle (2β) of an electron beam such that

$$l_t = \frac{\lambda}{2\beta} . \tag{12}$$

Here, λ is the wavelength of an electron beam. This can be derived simply by calculating the diameter of the region where a wave front perpendicular to an electron trajectory can be defined.

An extremely small value of 2β is, in principle, possible; this should lead to a large wave-packet width. However, the intensity of the electron beam becomes too weak in such a case for observation within a reasonable measurement time. Therefore the practical value of l_t is determined by the characteristics of the electron beam, i.e., how large a current density can be obtained under a small divergence angle. This feature is represented by brightness R, defined as current density per unit solid angle. The value depends on the kind of electron gun, and is invariant at any cross section of an electron beam that is not accelerated or decelerated. This invariance can be derived from Liouville's theorem (see, for example, Worster, 1969).

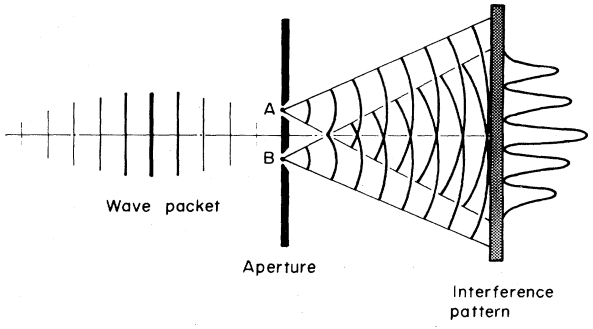

FIG. 6. Formation of interference pattern with electron wave packets. Interference pattern can be observed only when a wave packet interferes with itself.

The transverse coherence length l_t cannot be directly expressed by brightness R, since the relation depends on the enlarging electron-optical systems necessary for electron hologram recording. However, the maximum number N_t of observable interference fringes is independent of such experimental conditions (Tonomura, Matsuda, Endo, Todokoro, and Komoda, 1979). This number can be represented by brightness R from simple calculations (see Fig. 7):

$$N_t = \frac{\lambda}{s}\left[\frac{\pi R T_0}{J}\right]^{1/2} . \tag{13}$$

Here, s, J, and T_0 are the minimum fringe spacing recordable on film, charge density for sensitizing film, and exposure time, respectively.

The length of a wave packet is the longitudinal coherence length l_l, which is determined by uncertainty in wavelength ($\Delta\lambda$) or energy spread (ΔE) for an electron beam (Lenz and Wohland, 1984). That is

$$l_l = \frac{\lambda^2}{\Delta\lambda} = \frac{2E}{\Delta E}\cdot\lambda . \tag{14}$$

Here, E is the kinetic energy of an electron beam. This equation can be obtained by calculating the length of a wave packet consisting of sinusoidal waves with wavelengths distributed over $\Delta\lambda$. The length l_l can also be represented by N_l, the number of wavelengths contained in the wave packet, as given by

$$N_l = \frac{\lambda}{\Delta\lambda} = \frac{2E}{\Delta E} . \tag{15}$$

Since the coherence of an electron beam is completely

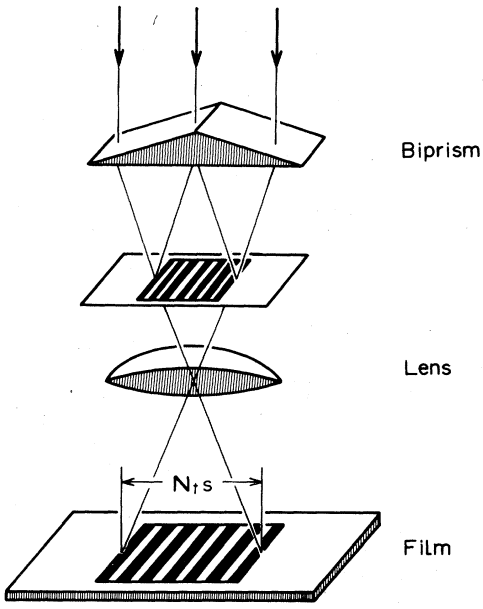

FIG. 7. Electron-optical arrangement for observing interference fringes.

determined by the kind of electron gun employed, we consider next the two characteristic coherence lengths of actual electron guns.

2. Thermionic cathode

Hairpin-type cathodes (see Fig. 8) are usually used in electron microscopy. Thermionic electrons are emitted from a tungsten filament 0.1 mm in diameter heated by applying an electric current. The emission current is controlled by a negative-bias voltage applied to the electrode (Wehnelt electrode) surrounding the filament. The emission area is, at the same time, limited only to the tip of the hairpin. Electrons having passed through the Wehnelt hole are accelerated to a desired voltage of, say, 100 kV. The beam has a minimum cross section called a crossover just after the hole. The diameter is a few tens of μm.

The brightness of this beam is 5×10^5 A/cm^2 sr at 100 kV. The energy spread is around 2 eV. The reason why the energy spread of an electron beam is larger than the theoretical value ($\sim$kT) by nearly 1 order of magnitude is that the energy spread anomalously increases during the electron acceleration due to electron-electron interactions; this is called the Boersch effect (Boersch, 1954).

By substituting these values into Eq. (13), we can calculate the number of observable interference fringes N_t as 180 when $s=20$ μm, $J=5\times10^{-11}$ C/cm^2, and $T_0=30$ sec. The longitudinal coherence length l_l and wave number N_l are 0.37 μm and 10^5, respectively. Therefore the maximum number of observable interference fringes can be seen to be limited by the transverse coherence length.

A pointed cathode was developed by Hibi (1956) for the purpose of realizing electron holography. Electrons are emitted from only the tip of a tungsten needle attached to a hairpin filament. The electron source size is a few μm. The brightness of the beam increases to $1-2\times10^6$ A/cm^2 sr at a 100-kV accelerating voltage, since the field-emission effect is added. The energy spread is as small as 1 eV.

These values lead to $N_t=250$, $l_l=0.74$ μm, and $N_l=2\times10^5$. This cathode has frequently been used for high-resolution electron microscopy; its beam characteristics are attractive in that not only is the illumination coherent, but the effect of some aberrations accompanying an electron lens decrease.

3. Field-emission cathode

The phenomenon of field emission was actually first discovered in the eighteenth century, and utilization in a field-emission microscope for observing a tip surface having an atomic-scale resolution took place early in this century (Müller, 1937). Nevertheless, it was Crewe *et al.* (1968) who developed a practical field-emission cathode. They used it as a source for a scanning transmission electron microscope, and greatly improved resolution down to atomic dimensions (Crewe, Wall, and Langmore, 1970).

The structure of a field-emission electron gun developed by Crewe *et al.* is shown in Fig. 9. Electrons are radially emitted from the hemispherical surface of a tip 1000 Å in radius. The virtual source size is less than 100 Å.

When an electric potential of 3—6 kV is applied between the tip and first anode, an emission current 1—100 μA is obtained. Only a few ($\sim$1/10 000) of the electrons pass through the first anode hole to be accelerated. The brightness of this beam is greater than that of a thermionic beam by 3 orders of magnitude, mainly because a strong electric field at the surface produces no space-charge effect under normal operating conditions. A typical measured value of brightness is 5×10^8 A/cm^2 sr. The energy spread of the beam is 0.3 eV when the emission current is 10 μA. The number of observable fringes calculated from these values is $N_t=4000$ and $N_l=10^6$.

Characteristics meeting the coherence requirements can be attained at the cost of elaborate techniques; an extremely thin tip has to be operated without any high-voltage discharge under an ambient pressure of 10^{-10} Torr.

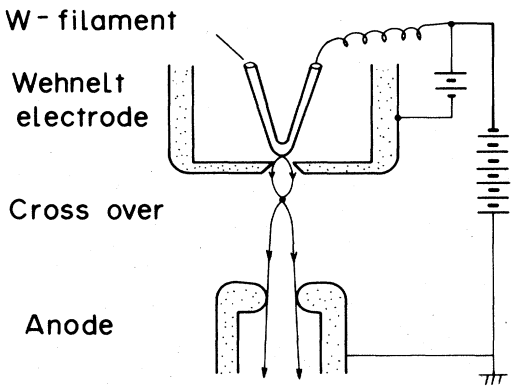

FIG. 8. Schematic for thermionic electron gun.

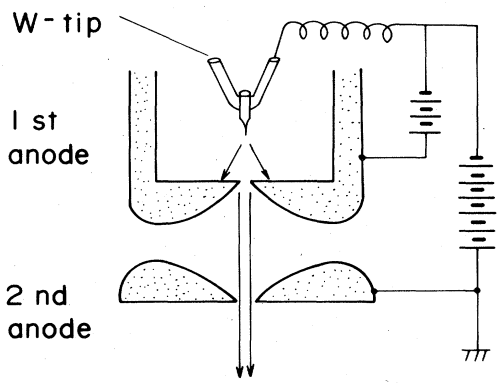

FIG. 9. Schematic for field-emission electron gun.

B. Interferometer

Electron interference fringes between two plane waves were first observed as an electron micrograph by Mitsuishi, Nagasaki, and Uyeda (1951). The fringes were attributed to the interference between two beams Bragg-reflected during passage through two crystalline thin films [see Fig. 10(a)].

Utilizing this principle, Marton (1952) observed interference fringes with three sheets of single crystalline films. A schematic of this setup is shown in Fig. 10(b). This was the first observation of artificially produced fringes with an interferometer. However, this interferometer was not practical, since it is virtually impossible to arrange three layers of thin films at will. It should be mentioned here, though, that this type of interferometer is now employed in neutron and x-ray interferometers.[3]

A practical interferometer was developed by Möllenstedt and Dücker (1955). This is an electrostatic biprism, which is composed of a fine filament bridged in the center and two plate-shaped electrodes with ground potential on both sides (Fig. 11). The diameter of the filament has to be small enough not to obscure the coherent region of an incident electron beam; ideally it should be less than 1 μm.

Several methods have been developed for producing such fine filaments. Usually a filament is produced by extending a burned rod of quartz, and its surfaces are covered with an evaporated gold layer. When a positive electric potential V_b of 10—100 V is applied to the filament, the electric potential $V(\rho)$ around the filament is logarithmic, such that

$$V(\rho)=V_b\frac{\ln(\rho/\rho_2)}{\ln(\rho_1/\rho_2)} . \tag{16}$$

Here, ρ_1 and ρ_2 are the filament radius and the distance from the filament center to the electrode, respectively.

If collimated electrons are incident on both sides of the filament, they are slightly attracted toward the filament. The deflection angle δ can be calculated when small to be

$$\delta=\frac{\pi e V_b}{2E\ln(\rho_1/\rho_2)} . \tag{17}$$

Here, E is the kinetic energy of an electron. This equation signifies that the deflection angle is constant, independent of the incident position of an electron. Moreover, it is proportional to the voltage applied to the filament. This indicates that the biprism is a precise electron version of an optical biprism.

Magnetic versions of an electron biprism have also been investigated (see Fig. 12; Krimmel, 1960; Boersch, 1960). However, they have not proven to be as practical as the electrostatic device.

[3]Details of neutron interferometers and their applications are described, for example, by Klein and Werner (1983).

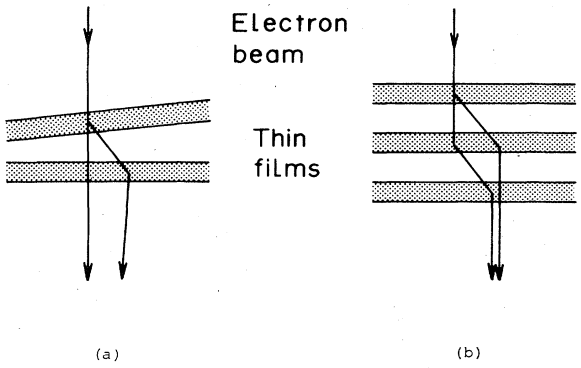

FIG. 10. Interference fringes formed with single-crystalline thin films: (a) two films; (b) three films.

C. Electron lens

Although optical lenses have been employed since the thirteenth century, electron lenses were not invented until 1926 (Busch, 1926). Electron lenses are classified into two types: electrostatic and magnetic lenses. Both types were widely used for different purposes. In modern electron microscopes, magnetic lenses are usually employed, mainly due to their small aberration rates.

An example of a magnetic lens is shown in Fig. 13. The key component is a circular coil, through which magnetic flux flows. The coil is surrounded by a toroidal iron

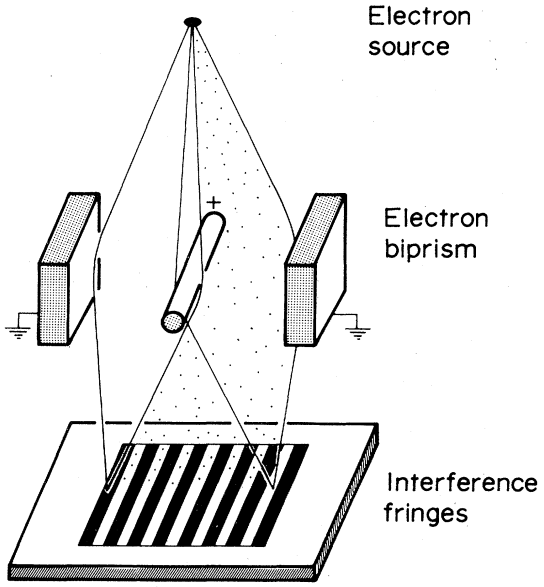

FIG. 11. Schematic of Möllenstedt-type electron biprism. The biprism consists of a central fine filament and two electrodes on both sides. Two electron beams traveling on both sides of the filament are attracted towards the filament by the application of a positive potential to it, and overlapped to form an interference pattern in the lower plane.

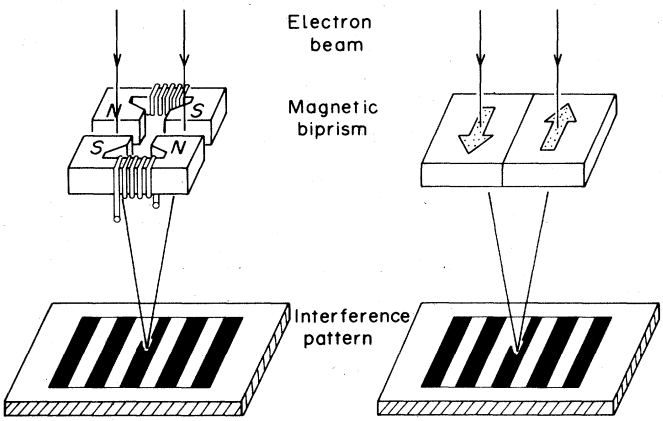

FIG. 12. Schematic of magnetic electron biprism (Krimmel, 1960, and Boersch, 1960).

yoke, which has a gap inside. Magnetic flux flowing through the yoke leaks outside at the gap. The leakage fields are axial symmetric and function as a lens for electrons. This will be made clearer by the following simple explanations.

Parallel electrons are incident along the axis of the axial-symmetric magnetic fields (see Fig. 14). An off-axis electron first interacts with the radial component $B_r(z)$ of the magnetic field and receives the Lorentz force $-ev_z B_r(z)$ in the direction perpendicular to the meridional plane, where $B_r(z)$ is given, in terms of magnetic field on axis $B(z)$ by

$$B_r(z) = -\frac{r}{2}\frac{dB(z)}{dz} . \tag{18}$$

Using this equation and $v_z = dz/dt$, we can express the force as $(er/2)[dB(z)/dt]$. This means that angular velocity $\dot{\varphi}$ can be given by $eB(z)/2m$. Electrons with a velocity involving a rotational component around the axis

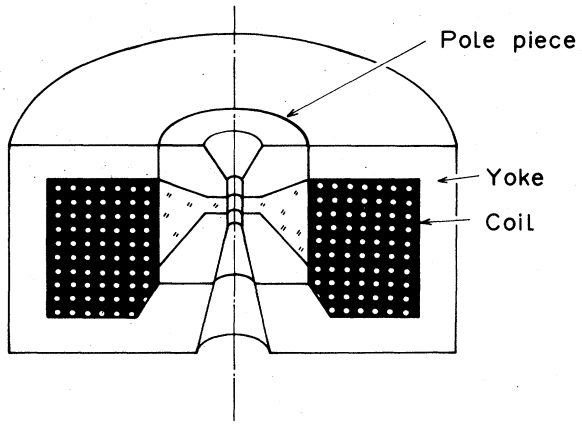

FIG. 13. Cross section of electron lens. The magnetic lens consists of axial-symmetric magnetic fields that are produced from the gap of the iron yoke.

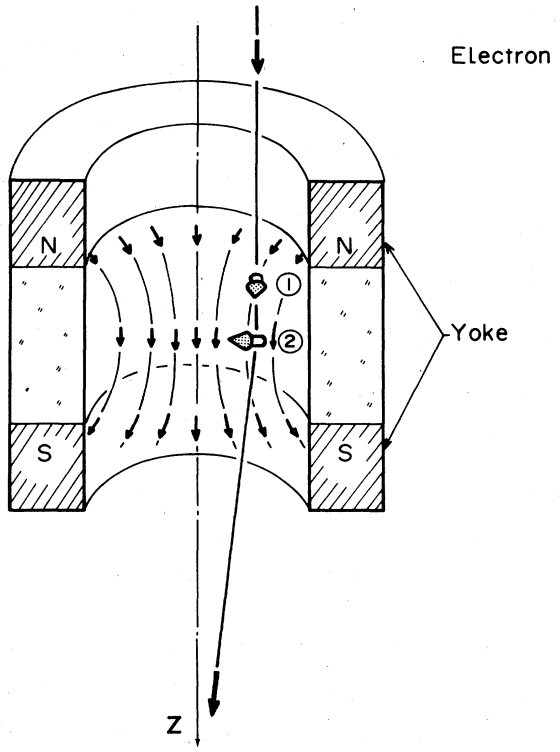

FIG. 14. Focusing action of electron lens. An incident electron is first deflected by the radial component of the magnetic field in the direction perpendicular to the figure plane, as indicated by arrow (1), and then deflected by the axial magnetic field towards the axis, as indicated by arrow (2), which forms a lens action.

then interact with the axial magnetic field $B(z)$ and are deflected toward the axis. Since this force is represented by $-(e^2r/2m)B(z)^2$, the equation of motion can be written as

$$m\frac{d^2r}{dt^2} = -\frac{e^2r}{2m}B(z)^2 + \frac{m(r\dot{\varphi})^2}{r} = -\frac{e^2r}{4m}B(z)^2 . \tag{19}$$

It can be concluded from this equation that a paraxial electron is always subject to force toward the axis. Since a trajectory multiplied by a constant factor is also a solution of Eq. (19), all electrons starting from a point are focused onto an image point, which means a convex lens action. A concave lens cannot be obtained even if $B(z)$ is replaced by $-B(z)$ because of the quadratic factor $B(z)^2$ in Eq. (19). This is the reason why aberrations in an electron microscope cannot be compensated for by a combination of convex and concave lenses, and why they determine the resolution.[4]

[4]Here, we should recall that Gabor's original objective in devising holography was to improve the resolution of electron microscopes via optical means.

It has been clarified that axial-symmetric magnetic fields form a lens action for paraxial electrons, which travel near the optic axis as well as at a small angle to it. As a result, the intensity distribution in an object plane is reproduced in the image plane. At this juncture, it must also be confirmed that the phase distribution is reproduced in the image plane. This can be simply shown in an optical case: path lengths are the same for all rays starting from an object point and arriving at its conjugate point.

In other words, a spherical wave diverging from an object is transformed into a spherical wave converging to an image point. In the electron case, the situation is a little more complicated; electron motion in magnetic fields is not confined to a meridional plane, but is along a spiral. Wave fronts defined as perpendicular to electron trajectories are also spiral. In spite of such circumstances, it can be verified that phase differences vanish for all trajectories from an object point to its conjugate. Therefore the phase distribution of an electron wave at an object plane is assured of being reproducible at the image plane.

III. HISTORICAL DEVELOPMENT OF ELECTRON HOLOGRAPHY

Let us now take a brief look at experimental attempts at holography. Practical applications to fields of technological endeavor will be introduced collectively in Sec. VI.

A. Early experiments

The original approach that Gabor took was an in-line projection method (Gabor, 1949). This differs from the conventional transmission method, which was later proposed by Haine and Dyson (1950) as more practical for an electron microscope (see Sec. I).

In the projection method, an object is illuminated with a divergent spherical wave from a point focus close to the object, rather than with a plane wave. Its hologram is then formed as a highly magnified projected interference pattern between object and transmitted waves. No lenses are used (see Fig. 15). This method requires a very small electron point focus. The diameter in this case determines the resolution of the reconstructed images.

Since it was technically difficult in Gabor's time to realize a fine enough probe, the transmission method was subsequently devised so that holograms could be easily formed in electron microscopes. These holograms can be said to be defocused electron micrographs photographed under coherent illumination. Such a micrograph was already possible even in those days. Fresnel fringes in a greatly defocused photograph of a specimen edge (see Fig. 16) had been reported by Boersch (1940).

Although the feasibility of holography was demonstrated in optical experiments by Gabor (1949), Rogers (1951), Baez (1952), and Kirkpatrick and El-Sum (1956), the first true experiment on electron holography was carried out by Haine and Mulvey (1952). They formed a hologram as a defocused image of zinc-oxide crystals [see Fig. 17(a)] in which Fresnel fringes from crystal edges could be observed. The reconstructed image shown in Fig. 17(b) is still accompanied by Fresnel fringes with wider spacings that come from the conjugate image. Nevertheless, the

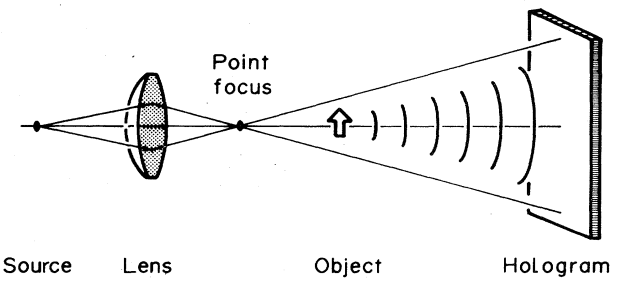

FIG. 15. Projection method for in-line holography. An electron hologram is formed as a projected interference pattern between the spherical wave from a point focus and the scattered wave from an object.

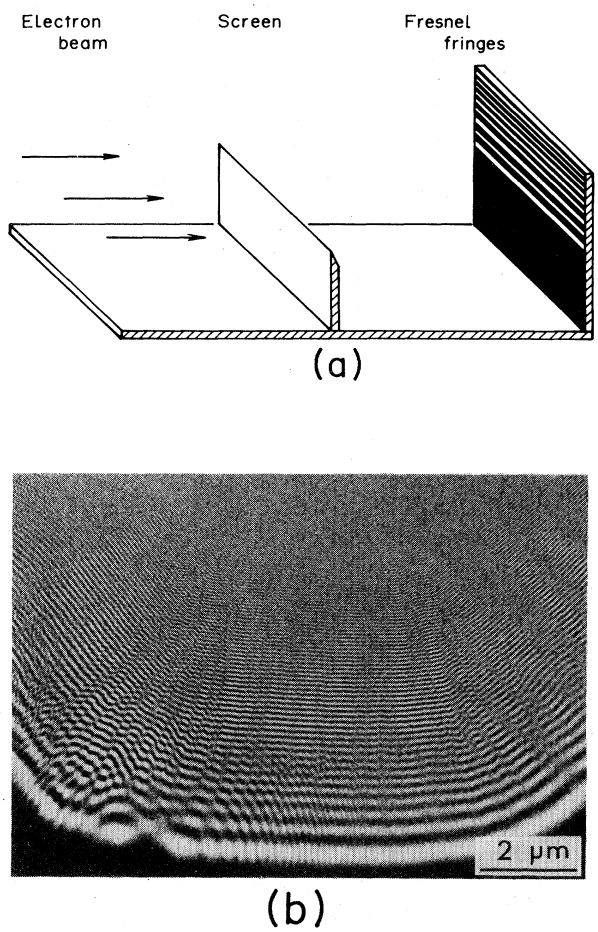

FIG. 16. Formation of Fresnel fringes, i.e., greatly defocused image of a screen edge: (a) schematic; (b) Fresnel fringes.

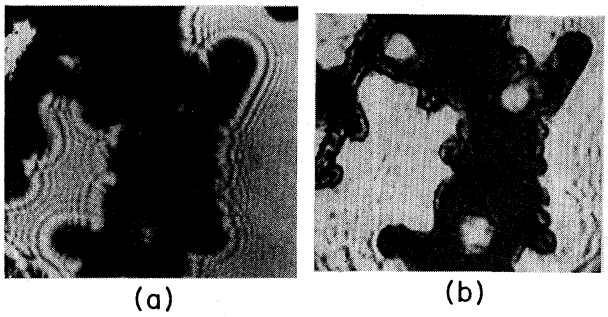

FIG. 17. Image reconstruction of zinc-oxide crystals (Haine and Mulvey, 1952): (a) electron hologram; (b) reconstructed image. An optical image was reconstructed from an in-line electron hologram for the first time, although the image was disturbed by Fresnel fringes that were produced from its conjugate image.

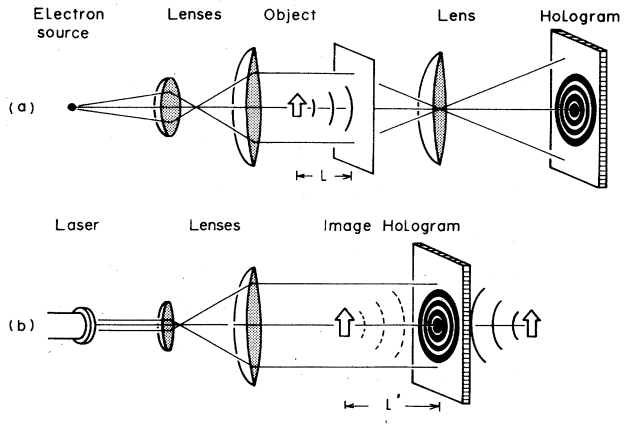

FIG. 18. Experimental processes of Fraunhofer in-line holography: (a) hologram formation; (b) image reconstruction.

reconstruction can be said to be verified, even if not perfectly.

Similar results were obtained by Hibi (1956). He developed a pointed cathode as a coherent electron source for realizing electron holography. He then proceeded to reconstruct images from Fresnel-fringe-like holograms formed using a pointed cathode.

B. In-line holography

1. Experimental trials

Although the reconstruction of clear images was demonstrated using off-axis laser holography by Leith and Upatnieks (1962), DeVelis, Parrent, and Thompson (1966) also showed that, even via in-line holography, an image reconstruction free from disturbance is possible if holograms are formed in a Fraunhofer diffraction plane of an object.

An electron version of this experiment was carried out by Tonomura, Fukuhara, Watanabe, and Komoda (1968). In this experiment, a 100-kV electron microscope equipped with a pointed cathode was used (λ: 0.037 Å). The electron-optical system for hologram formation is shown in Fig. 18(a). An electron beam from the source was focused through the first condenser lens and then collimated to illuminate a specimen through the second condenser lens. Small objects surrounded by clear spaces were selected as specimens so that the transmitted electron wave might be regarded as a coherent background. The diffraction pattern of a specimen at a plane 2 mm distant from it was magnified 3000—6000 times by electron lenses and recorded on film. Since the illumination angle (2β) was made as small as 1×10^{-6} (rad), the low current density necessitated a long exposure time of up to 10 min. The film was reversed with high contrast and was regarded as a hologram.

Optical reconstruction was carried out using a He-Ne laser (λ': 6328 Å) as shown in Fig. 18(b). Just as in the hologram formation process, a light from the laser was focused and collimated through two lenses with short and long focal lengths to illuminate an electron hologram. Two images were reconstructed at planes $l'=m^2(\lambda/\lambda')l$ distant from the hologram. Under conditions of $l=2$ mm, $\lambda=0.037$ Å, $\lambda'=6328$ Å, and $m=3000$, l' can be calculated to be around 10 cm.

An example of the reconstruction is shown in Fig. 19. The object is fine gold particles placed on a thin carbon film. The diameter of the smaller particles is around 100 Å. Carbon film is employed as a transparent supporting film. The hologram in Fig. 19(a) looks like an overlapped pattern of concentric interference fringes (zone plates); it is impossible to imagine the shape of the original object only by looking at its hologram. This feature comes from the Fraunhofer condition (see Fig. 2). In actuality the distance l of 2 mm from object to hologram is sufficiently large compared with $a^2/\lambda=25$ μm to satisfy Eq. (5).

This Fraunhofer condition negates the image distur-

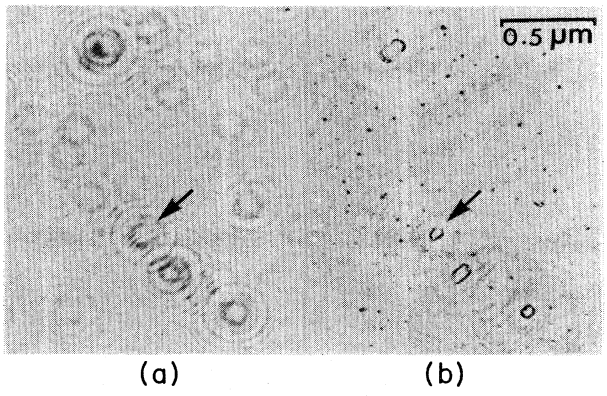

FIG. 19. Image reconstruction of fine gold particles (Tonomura, Fukuhara, Watanabe, and Komoda, 1968): (a) electron hologram; (b) reconstructed image. A clear-cut image was reconstructed free from the disturbances due to the conjugate image, since Fraunhofer holography was adopted.

bance due to the conjugate image, as can be seen in Fig. 19(b). This is because the conjugate image is spread out at the plane of the reconstructed image over a region of diameter $\sqrt{2\lambda l}$, which is much larger than the object size a under the Fraunhofer condition (Fig. 2). (It should be noticed here that lengths are reduced to those in the hologram formation stage in an electron microscope.)

Another example is shown in Fig. 20, where the specimen is a zinc-oxide crystal. Since the size of the whole crystal is 5000 Å, the Fraunhofer condition is not satisfied. This can be recognized merely by looking at the hologram in Fig. 20(a), since the interference fringes are completely different from those of a zone plate. However, the needles of the crystal are reconstructed without any disturbance because the needle diameter is small enough to satisfy the Fraunhofer condition. The positions of the needle tips could also be determined in three dimensions by measuring the focusing position of each tip.

2. Image resolution

The resolution of reconstructed images, d, in this experiment was a few tens of Å. This value is determined by the diameter D of a zone plate recorded on a hologram,

$$d=1.6\frac{\lambda l}{D} . \tag{20}$$

This equation is equivalent to the formula giving the resolution of a lens, a natural consequence because a zone plate performs as a lens. The diameter of a zone plate may be limited by film resolution. However, in that case, hologram magnification can be made larger. Under the appropriate conditions, D is determined by the transverse coherence length l_t given by Eq. (12). Consequently, the resolution d can be represented as

$$d=3.2\beta l . \tag{21}$$

This indicates that high resolution can be attained under conditions of a small β and l, though at the cost of clearance from the conjugate image. In this experiment, d is calculated to be 30 Å, which is consistent with the experimental data.

Hanszen theoretically investigated the contrast transfer function of holographic imaging and proposed a method for improving electron microscope resolution (Hanszen, 1970). The transfer function of in-line holography is the square of that for an electron lens. This negates the contrast inversion that always accompanies a highly magnified electron micrograph in some spatial frequencies due to spherical aberration in the electron lens. The remaining problem of frequency gaps can also be removed by superposing several images with different defocusings, the transfer intervals of which replenish each other.

The resolution of reconstructed images was improved by Munch (1975) using a field-emission electron beam. The high brightness of this electron beam permitted a decrease in the illumination angle, 2β. In addition, finer particles were selected as samples, thereby allowing a smaller sample-hologram distance l. A resolution of 10 Å was achieved under conditions of $l=5$ μm (see Fig. 21). Munch concluded that higher-resolution imaging was difficult with in-line holography, since the contrast of a zone plate was extremely low due to the weak intensity of the scattered wave from a small object. Bonnet, Troyon, and Gallion (1978) also employed a field-emission electron beam to obtain an image resolution of 7 Å.

The in-line holography described up to now entails several limitations, such as a small size for objects surrounded by clear spaces. However, the coherence conditions for an illuminating electron beam are much less stringent than those for off-axis holography. Consequently in-line holography is well suited to such specimens as isolated fine particles, although there are still problems with regard to the supporting film for production of a coherent background wave.

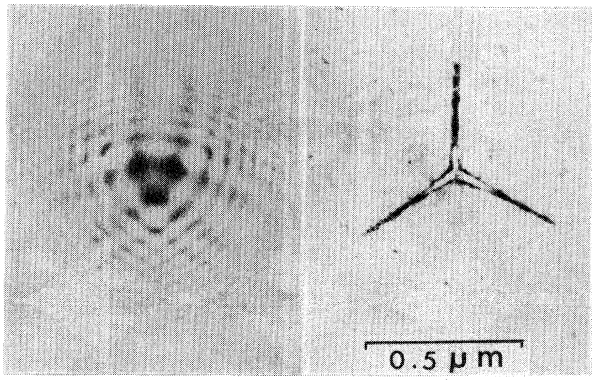

FIG. 20. Image reconstruction of zinc-oxide crystal (Tonomura, Fukuhara, Watanabe, and Komoda, 1968): (a) electron hologram; (b) reconstructed image. Although the size of the whole crystal is too large to satisy the Fraunhofer condition, the needles of the crystal are thin enough to be reconstructed without the conjugate image disturbances.

C. Off-axis holography

Off-axis Fresnel electron holography was first carried out by Möllenstedt and Wahl (1968). A slit-shaped electron source was employed to record as many biprism interference fringes as possible on film. An image of a thin tungsten filament was optically reconstructed as shown in Fig. 22. The reconstructed image is resolved only in a direction perpendicular to the filament. Tonomura (1969) subsequently carried out a trial using single-crystalline thin film as a beam splitter, and reconstructed an image.

Weingärtner, Mirandé, and Menzel (1969) theoretically predicted the possible attainment of an image resolution as high as 0.4 Å by adopting off-axis image holography. The influence of the illumination angle of an electron

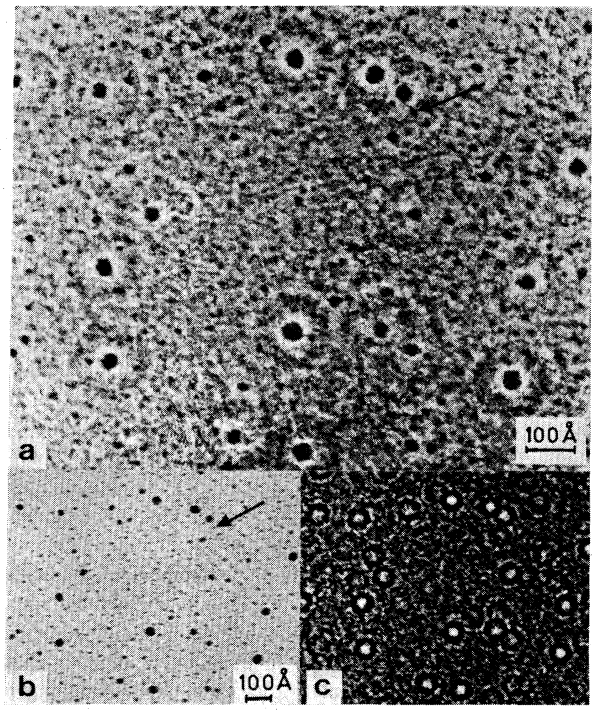

FIG. 21. Image reconstruction of fine gold particles (Munch, 1975): (a) reconstructed image; (b) electron micrograph; (c) electron hologram. An image resolution of 10 Å could be obtained by using both a field-emission electron beam and fine-particle specimens.

beam on image resolution was thought by them to be smaller than that for any other arrangement in off-axis holography. The spherical aberration of an electron lens is compensated for in the reconstruction stage by that of an optical concave lens to improve resolution.

Improvement of a reconstructed image was reported by Tomita, Matsuda, and Komoda (1970, 1972; see Fig. 23) and Saxon (1972) using off-axis Fresnel holography. The former used a pointed cathode and the latter a field-emission electron gun as the electron source. Saxon further demonstrated how to correct coma aberrations in an electron lens during the optical reconstruction stage.

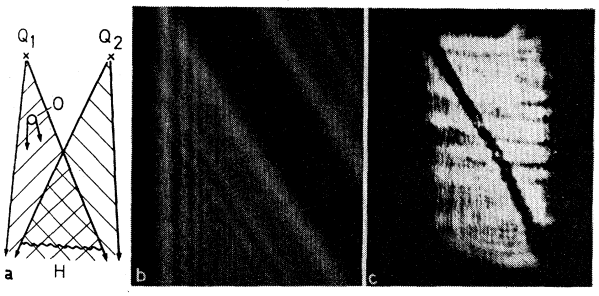

FIG. 22. Image reconstruction of thin tungsten filament (Möllenstedt and Wahl, 1968): (a) schematic for hologram formation; (b) electron hologram; (c) reconstructed image. An optical image was reconstructed from an off-axis one-dimensional electron hologram for the first time.

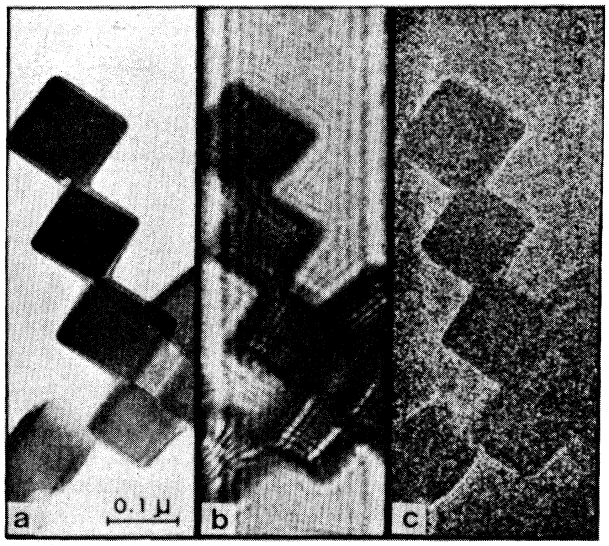

FIG. 23. Image reconstruction of magnesium-oxide particles (Tomita, Matsuda, and Komoda, 1970): (a) electron micrograph; (b) electron hologram; (c) reconstructed image. An optical image was reconstructed from an off-axis Fresnel hologram.

Image quality was greatly improved by Tonomura, Matsuda, Endo, Todokoro, and Komoda (1979) using a field-emission electron beam that could produce 3000 biprism fringes instead of the former 300 (the number of carrier fringes in a hologram corresponds to that of picture elements). Using this electron beam, they found that lattice fringes of gold {111} planes (spacing: 2.4 Å) could be reconstructed, together with half-spacing fringes (Tonomura, Matsuda, and Endo, 1979). Thus even Bragg-reflected beams could be optically reconstructed, and the resolution of a reconstructed image became comparable to that of an electron microscopic image (see Fig. 24). Lichte (1985) could reconstruct high-contrast lattice fringes of carbon black (spacing: 3.4 Å) with much narrower hologram interference fringes (spacing: 0.8 Å) than for lattice fringes.

Off-axis holography without use of an electron biprism was investigated by Matteucci, Missiroli, and Pozzi (1982). A single-crystalline film was employed as a wave-front-division beam splitter. An electron beam incident on the film excites the Bragg reflection to split into two (transmitted and reflected) beams. When an object is placed in the path of one of the two beams, a lattice image modulated by the object is formed at the image plane of an electron lens. This image can then be regarded as an off-axis Fresnel hologram. The coherence conditions of an illuminating electron beam are less stringent than those for an electron biprism. Consequently holograms can be formed using even an electron beam from a pointed cathode.

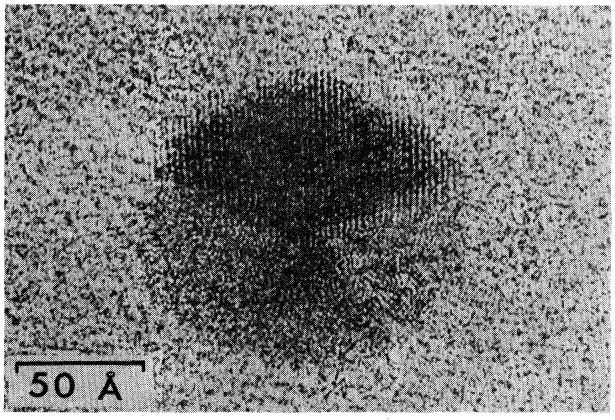

FIG. 24. Reconstructed lattice fringes in a fine gold particle (Tonomura, Matsuda, and Endo, 1979). The lattice resolution of reconstructed images was improved up to 1.2 Å by using a field-emission electron beam; even Bragg-reflected electron beams could be optically reconstructed.

One more interesting method is Fourier-transform holography, which was undertaken by Lauer (1984). A weak-scattering foil was placed at the normal specimen position of an electron microscope, and an object at the back focal position of the objective lens (see Fig. 25). The object was restricted to one-half the focal plane; the other half was screened off by a mask. The resolution of reconstructed images was 30 Å.

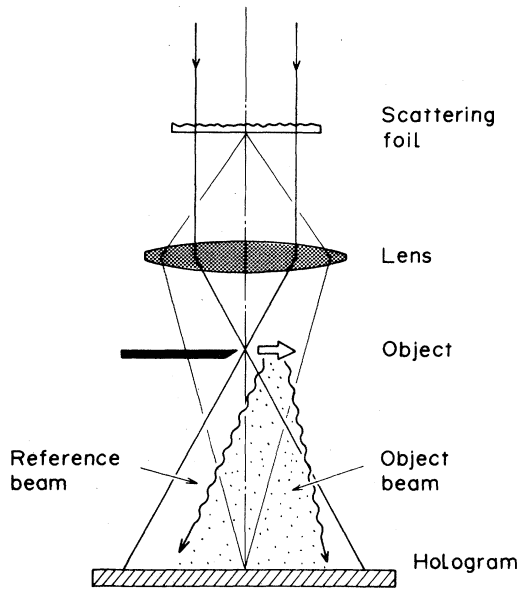

FIG. 25. Electron-optical arrangement for forming Fourier-transform hologram. A hologram is formed as an interference pattern between a spherical wave from a point source and the scattered wave from a specimen situated in the source plane.

IV. HOLOGRAPHIC TECHNIQUES FOR DISPLAYING PHASE DISTRIBUTION

The recent development of a field-emission electron beam has made the resolution of a holographically reconstructed image comparable to that of an electron microscope. However, unless new information can be obtained, there is no point in making a hologram that is inherently more difficult to create than an electron micrograph.

Actually, utilization of the electron phase distribution does provide new information. Phase information is, in principle, observable via electron microscopes with use of an electron biprism. However, it is much more convenient to display phase distribution using optical techniques in the optical reconstruction stage of electron holography.

Several techniques are available for observing phase distribution. Among them, interference microscopy is most commonly used in optical fields. The contour map of a wave front of light transmitted through an object is displayed by overlapping a plane wave onto the object wave. An electron version of interference microscopy can easily be realized once the electron wave front is optically reconstructed. A typical interference electron microscopy approach will be outlined in the following subsections.

A. Hologram formation

In the first step, an off-axis image hologram is formed in an electron microscope where a field-emission electron gun and electron biprism are installed. A schematic diagram for hologram formation is shown in Fig. 26. A specimen is situated in only one-half of the specimen plane. A collimated electron beam illuminates it, and the image is formed through the objective lens. A reference beam passing through the other half reaches the image without disturbance from the specimen. These two beams are superimposed to form an interference pattern with an electron biprism, and further enlarged using magnifying electron lenses. They are then recorded on film as an image hologram.

B. Optical reconstruction for interference microscopy

An optical reconstruction system is shown in Fig. 27. As shown there, an electron hologram is illuminated with a collimated laser beam. An image is reconstructed in one of the two diffracted beams, and is formed again through two lenses onto the observation plane. A collimated laser beam is split by a half-silvered mirror. The beam is then sent to the observation plane via a separate path to form the interference pattern between the object wave and reference wave, i.e., to form the interference micrograph. Although this interference micrograph is formed with the help of optical devices, it can be regarded as a pure "electron" interference micrograph. This is because there are no differences in interference patterns be-

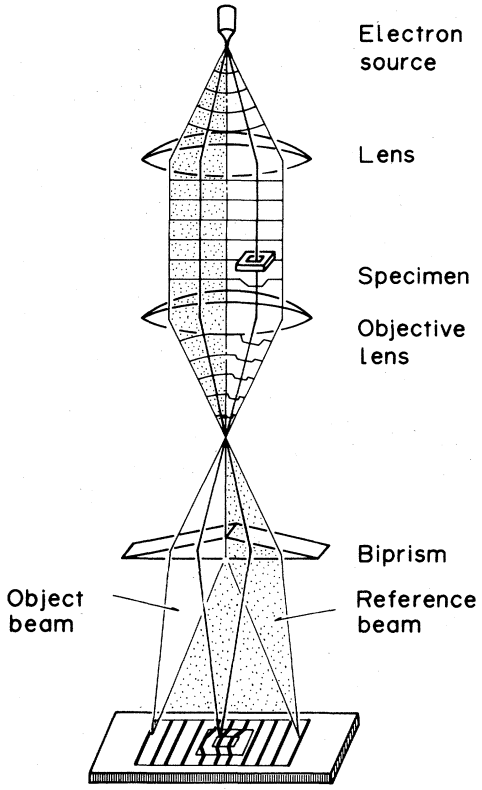

FIG. 26. Schematic for forming off-axis hologram. A specimen is located in only one-half of the specimen plane, and the other half is for a reference beam. The transmitted beam through the specimen and the reference beam are overlapped with the biprism to form a hologram.

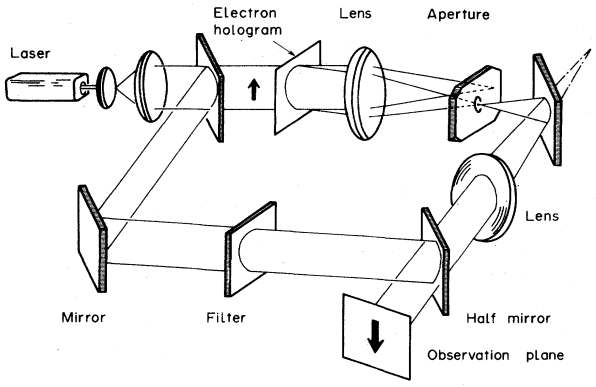

FIG. 27. Optical reconstruction system for interference microscopy. A collimated laser beam illuminates the hologram to reconstruct an image, which is formed again through two lenses on the observation plane. A laser beam split by a half mirror is sent to the plane to form an interference image.

tween electron and light waves if all the dimensions are counted in wavelength units.

C. Techniques for phase-difference amplification

The electron phase shift is, in some cases, less than a wavelength. Consequently even a single contour line cannot be observed in an interference micrograph. Such circumstances are not rare in electron interferometry. An example of an optical reconstruction system in such a case is shown in Fig. 28. Holographic techniques can be effectively employed.[5] A collimated laser beam is split into two by a Mach-Zehnder interferometer to produce two coherent beams propagating in slightly different directions. They illuminate an electron hologram and form a pair consisting of a reconstructed image and its conjugate. A reconstructed image of one beam and a conjugate image of the other beam are overlapped on the observation plane by passing through an aperture.

A conventional interference micrograph is an interference pattern between a reconstructed image and a plane wave. The phase difference between the twin images is twice the value of the conventional interference micrograph. This is because the amplitudes of the twin images are complex conjugate with each other; i.e., the phase values are opposite in sign. Thus the obtained interference micrograph looks as if the phase distribution is amplified by 2 times.

What should be done when the 2-times amplified phase distribution is still too small to be observed? One way around this difficulty is to repeat the amplification process many times. Another is to utilize the higher-order diffracted beams from a high-contrast hologram. The principle behind the former method is easily understood. Thus only that for the latter method will be described here.

The intensity $I(x,y)$ of the interference pattern between an object wave and tilted plane wave can be calculated similarly to Eq. (7). It looks like

$$I(x,y)=1+\varepsilon\sin[\psi(x,y)+k\alpha y]\ , \tag{22}$$

where $\psi(x,y)$ expresses the phase distribution of an object wave. If ε is smaller than unity, the transmittance $t(x,y)$ of a hologram recorded with contrast γ [see Eq. (1)] is expanded in a power series,

$$t(x,y)=1-\frac{\gamma}{2}\varepsilon\sin Q+\frac{\gamma(\gamma+2)}{8}\varepsilon^2\sin^2 Q - \frac{\gamma(\gamma+2)(\gamma+4)}{48}\varepsilon^3\sin^3 Q+\cdots\ , \tag{23}$$

where $Q=\psi(x,y)+k\alpha y$.

[5]This technique was developed for optical applications by Matsumoto and Takahashi (1970) and applied to electron holography by Endo, Matsuda, and Tonomura (1979).

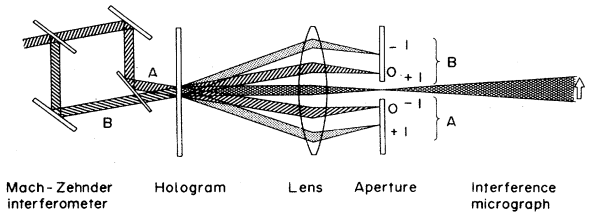

FIG. 28. Optical reconstruction system for phase amplified interference microscopy. Two coherent laser beams illuminate the hologram so that a reconstructed image of beam A and a conjugate image of beam B may be overlapped to form a two-times phase-amplified interference micrograph.

If $\gamma=-2$, then all the terms vanish except the first and second. That means only $\pm$first-order diffracted beams expressed by $e^{\pm iQ}$ are produced when the hologram is illuminated with a plane wave. However, when $|\gamma| \gg 2$, the higher-order terms cannot be neglected. The term $\sin^n Q$ contains factors $e^{\pm inQ}$, which correspond to $\pm n$th-order diffracted beams. Therefore, in the nth-order beam, the phase distribution is amplified n times, as is the inclination angle α. Thus the phase distribution of a reconstructed image formed with the nth-order diffracted beam is n times as large as that of the original image $\psi(x,y)$.

If a reconstructed image in the nth-order diffracted beam and a conjugate image in the mth-order beam are overlapped to form an interference micrograph, the resultant amplification can then be given by $m+n$. This amplified interference micrograph can actually be obtained using the optical system shown in Fig. 28, if the angles of incidence of the two illuminating beams onto the hologram are adjusted.

Up to now, maximum amplification rates of 16 and 10 times have been reported in optical and electron holography, respectively. With the former method of repeated hologram formation, 32-times amplification has recently been reported (Endo *et al.*, 1984). Further technical details will be reported in Sec. VI, with particular attention to applications to thickness measurement.

V. INTERPRETATION OF INTERFERENCE ELECTRON MICROGRAPHS

Before discussing the applications of interference electron microscopy, we need to consider briefly how interference micrographs are interpreted.

A. Electron beam phases

A simple review of the fundamental interaction between an electron beam and electromagnetic fields follows (a more detailed description was provided by Ehrenberg and Siday, 1949).

When an electron passes through electromagnetic fields $(\mathbf{E},\mathbf{B})$ with velocity $\mathbf{v}$, it is deflected by the Lorentz force $-e(\mathbf{E}+\mathbf{v}\times\mathbf{B})$. What kind of physical effects do electromagnetic fields have on the electron when it manifests wavelike behavior? The concept of force is no longer relevant; instead, that of "phase shift" comes into play. Electromagnetic fields $\mathbf{E}$ and $\mathbf{B}$ take on a secondary physical meaning, since they were originally defined as forces acting on a unit charge. The primary physical entities are the electromagnetic potentials V and $\mathbf{A}$, which are directly related to the phase shift.

If electromagnetic fields are weak enough for the WKB approximation to be valid, the phase S of an electron wave function can be derived from the Schrödinger equation as follows:

$$S=\frac{1}{\hbar}\int(m\mathbf{v}-e\mathbf{A})d\mathbf{s}\ , \tag{24}$$

where the integral is carried out along an electron path. Conversely, this can be considered to give a definition of electromagnetic potentials.

It is not difficult to understand from Eq. (24) what kind of influences electromagnetic potentials have on the electron phase. The first term, $\int m\mathbf{v}\,d\mathbf{s}/\hbar$, in this equation corresponds to the optical path length, where the effect of electrostatic potentials is included. The effect of vector potentials cannot be explained in this form, and is given by the second term. If these two terms are compared, $-e\mathbf{A}$ may be interpreted as if it represented a kind of electron momentum. In exact terms, $-e\mathbf{A}$ is a momentum exchanged between sources of fields and an electron, and exists only because an electron has an electric charge, irrespective of whether it is at rest or moving (see Gingras, 1980). In fact, if a unit charge is placed in a magnetic field, the integral value of the field momentum (the vector product between electric and magnetic fields) over all the space becomes equal to the vector potential $\mathbf{A}$ at the point of the charge.[6] Furthermore, there is also an "Aharonov-Bohm effect," whereby an electron beam having passed through field-free regions is physically influenced by vector potentials (potential field momenta). Details of this effect will be touched upon in Sec. VI. Although vector potentials have an arbitrariness of gauge transformation, it does not follow that they have no physical significance.

B. Interpretation of contour maps

1. Classical treatment

An electron beam that has passed through electromagnetic fields picks up information about the fields in the form of a phase distribution. Although a variety of phase

[6]This is valid only when the Coulomb gauge is selected such that div $\mathbf{A}=0$; see Konopinski (1978).

values can result from the gauge transformation, the phase of an electron beam cannot be measured except by making two beams interfere with each other. Consequently the measured value is always a "phase difference" between them, which is independent of the choice of gauge.

A simple case is illustrated in Fig. 29, where an electron beam passes through uniform electromagnetic fields. Incident electrons are parallel, and consequently regarded as a plane wave if the wave front is assumed to be perpendicular to the trajectories, as in the case of light optics. The electrons are deflected by a uniform electric or magnetic field, and therefore the corresponding wave front is an inclined plane with the right side up. A virtual plane wave drawn with dotted lines in the figure is overlapped on this wave to form an interference pattern, which represents the contour map of this wave front.

The contour lines obtained in electric and magnetic cases are along equipotential lines and magnetic lines of force, respectively. This results from the fact that an electric or magnetic field rotates an incident wave front along the axis determined by an equipotential line or magnetic line of force. The height of the resultant wave front is always the same along the rotation axis. Thus a very simple conclusion can be drawn that the contour fringes in interference micrographs represent equipotential lines or magnetic lines of force, as viewed from the direction of the electron beam.

This is valid not only for a uniform field, as shown in Fig. 29, but also for an arbitrarily winding field. In addition, the magnetic flux contained between two adjacent contour lines can be calculated to be a constant value of h/e ($=4.1\times10^{-15}$ Wb). It is surprising that this relation holds for any velocity of an incident electron beam.

With an electric field, however, such a simple relation cannot be obtained. Some readers may worry about the asymmetry between electricity and magnetism. If a monopole beam instead of an electron beam can be utilized for interference microscopy, a constant electric flux of e is contained between two adjacent contour lines, irrespective of the monopole energy.

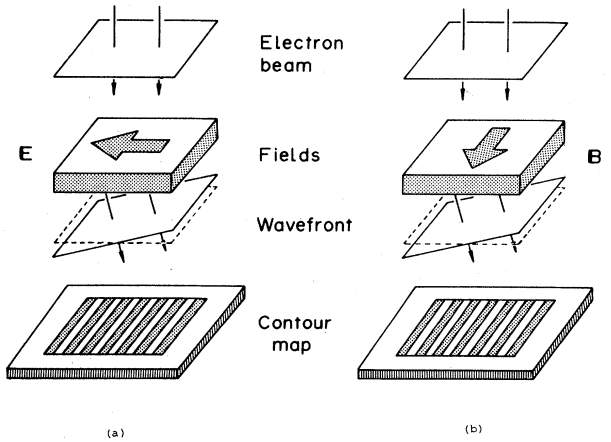

FIG. 29. Principle involved in electron interferometry observation of electromagnetic fields: (a) electric field; (b) magnetic field.

2. Quantum-mechanical treatment

The explanations up to now have been intuitive and not always exact. Although the main conclusions obtained have later been proven to be correct, this intuitive approach is bound to lead to inconsistencies. Actually, the existence of the Aharonov-Bohm effect (see Sec. VI.E) has been ignored.

Is there any inconsistency in a process by which electron trajectories are first determined and wave fronts are then drawn perpendicular to the trajectories? The fact is that the assumption is in general wrong that the wave front is perpendicular to electron trajectories. Here, one has to abandon intuitive thinking and return to the fundamental equation (24). The equation tells us that the wave front, i.e., equiphase surface, is perpendicular not to the direction of momentum $m\mathbf{v}$, but to that for generalized momentum, $m\mathbf{v}-e\mathbf{A}$. The spacing of adjacent wave fronts can no longer be given by de Broglie wavelength h/mv, but rather by $h/|m\mathbf{v}-e\mathbf{A}|$. The wave front thus defined also suffers from arbitrariness due to gauge transformation. However, this is not so crucial, since the wave front is not observable.

One point to be checked is whether the interpretation of phase contour maps remains unchanged when Eq. (24) is relied upon as a fundamental equation. The phase of an electron beam transmitted through electromagnetic fields can be calculated using Eq. (24). However, it cannot be determined uniquely due to the arbitrariness in the vector potential $\mathbf{A}$. Therefore the phase difference should always be considered as shown in Fig. 30. Two electron beams starting from a point source pass through a uniform electric or magnetic field at P_1 and P_2. They are brought together by a prism at another point where the phase difference ΔS is measured,

$$\Delta S=\frac{1}{\hbar}\oint(m\mathbf{v}-e\mathbf{A})d\mathbf{s}\ . \tag{25}$$

The line integral is carried out along a closed path determined by the two electron paths. The phase difference between two points, P_1 and P_2, at the exit plane of the field region can be regarded as given by ΔS.

With the electric field shown in Fig. 29(a), the phase difference can be expressed by

$$\Delta S=\frac{e}{\hbar}\int mv^2dt=\frac{e}{\hbar}\Delta V\cdot\tau\ . \tag{26}$$

Here ΔV is the difference in electrostatic potential between two points, P_1 and P_2, and τ is the transit time through the field region. In the case of a magnetic field,

$$\Delta S=-\frac{e}{\hbar}\oint\mathbf{A}\,d\mathbf{s}=-\frac{e}{\hbar}\int\mathbf{B}\,d\mathbf{S}\ , \tag{27}$$

where the surface integral is performed over the surface

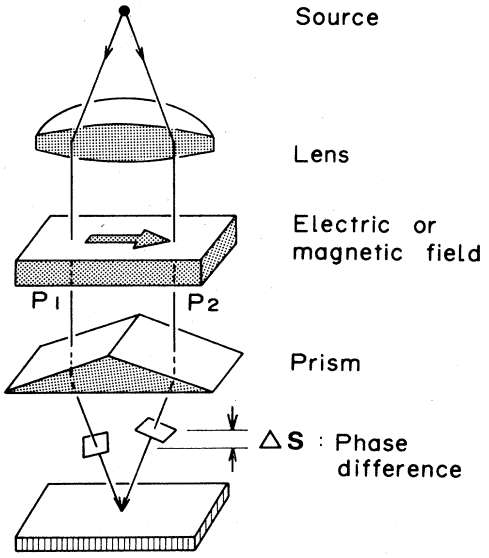

FIG. 30. Definition of phase difference. The phase difference between two points, P_1 and P_2, is given by the phase difference between two beams starting from a point, passing through the two points, and ending at another point.

bordered by the closed path. The following can be concluded from these two equations.

(1) The phase difference between two points, P_1 and P_2, vanishes when they are located along an equipotential line ($\Delta V=0$) or a magnetic line of force ($\int \mathbf{B}\,d\mathbf{S}=0$). Consequently the contour lines in the interference micrographs follow equipotential lines or magnetic lines of force.

(2) The phase difference of 2π is produced between two points, P_1 and P_2, when $\Delta V\cdot\tau=h/e$ or $\int \mathbf{B}\,d\mathbf{S}=h/e$.

These results assure that the contour fringes in interference micrographs can be intuitively interpreted as equipotential lines or magnetic lines of force.

3. Some complex cases

Before moving on, it would be useful to touch on a couple of slightly more complex cases. One is the case in which electric and magnetic fields are mixed. Such a case is often encountered in practical problems, for example, the observation of the magnetic domain structure of nonuniform ferromagnetic specimens. The contour fringes can be interpreted as neither magnetic lines of force nor thickness contour lines. A solution to this problem is to derive an additional hologram for a specimen where the surface is turned over. If the direction of an incident beam is reversed, then the magnetic phase shift given by Eq. (25) changes in sign. This is because velocity $\mathbf{v}$ and trajectory $\mathbf{s}$ are reversed in sign due to the transformation, but vector potential $\mathbf{A}$ is not. Consequently the electric contribution is invariant, but the magnetic contribution is reversed in sign. A holographic technique can be effectively employed to undertake summation and subtraction of the two phase distributions. As a consequence, the electric and magnetic effects can be separately measured. This principle has actually been utilized to determine the magnetization distribution in a three-dimensional cobalt fine particle (Tonomura, Matsuda, Endo, Arii, and Mihama, 1986).

The other case is that in which magnetic or electric fields are not confined neatly in a plane perpendicular to the incident direction of an electron beam, but are distributed in three dimensions. To take an extreme case, if a rotational magnetic field is viewed perpendicular to the rotational axis by an electron beam, the phase shift of an electron beam is canceled out in passing through the field [see Fig. 31(a)]. Of course, rotational magnetic lines of force can be observed if an electron beam is incident along the axis [Fig. 31(b)].

VI. PRACTICAL APPLICATIONS TO TECHNOLOGICAL PROBLEMS

Applications of electron holography have only begun to be investigated; thus the number of fields is still extremely limited. Nevertheless, entirely new types and quantities of information about the microscopic world are starting to be obtained. This section will undertake a review of the major areas of practical application now opening up.

A. Measurement of electric potential distributions

Microscopic distributions of electric potentials can be observed by interference electron microscopy, though only a few investigations have been reported. Merli, Missiroli,

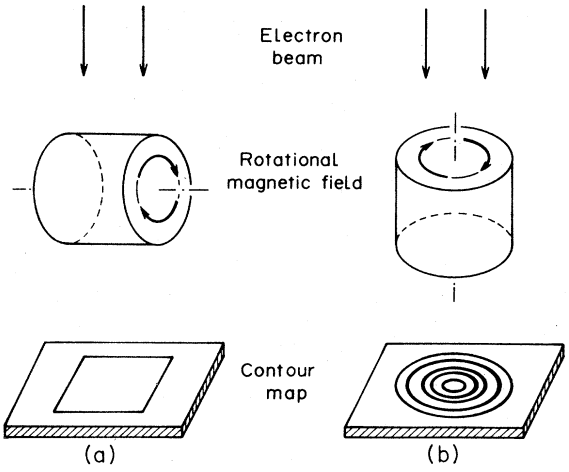

FIG. 31. Observation of rotational magnetic field by electron interferometry. Magnetic lines of force in three dimensions cannot be determined with a single interference micrograph viewed from one direction (a) or (b).

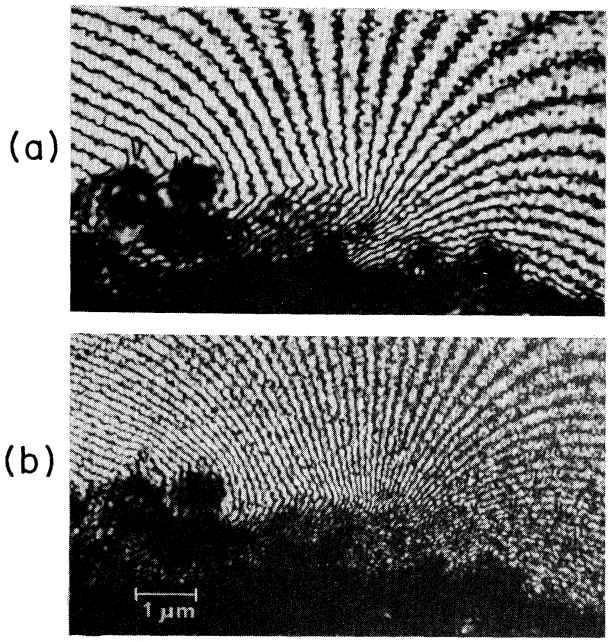

FIG. 32. Equipotential lines near p-n junction observed by electron interferometry (Frabboni, Matteucci, and Pozzi, 1985): (a) reverse bias = 4 V; (b) reverse bias = 8 V. Equipotential lines are directly observed as contour fringes.

and Pozzi (1974) tried to measure the distribution of electric potentials near the p-n junction and detected a phase shift in the high-field region as an interferogram. Kulyupin *et al.* (1978) measured the electric potential distribution near the apex of a field-emission tip, also by electron interferometry.

Holographic interference micrographs of the electric potentials near p-n junctions have recently been obtained by Frabboni, Matteucci, and Pozzi (1985) for the first time (see Fig. 32). Microscopic equipotential lines were observed for two values of the applied reverse bias voltages.

B. Thickness measurements

1. Interpretation of contour maps

The electric potential inside a specimen is higher than that in vacuum by 10—30 V. Consequently an electron beam is accelerated slightly and the wavelength becomes a little shorter in the specimen. This potential V_0 is called the inner potential, and each substance displays one that is characteristic, making it possible to measure the thickness distribution in a uniform specimen, as can easily be seen from Eq. (26). Since ΔV is replaced by constant V_0 and τ is proportional to the thickness, the contour lines in the interference micrograph indicate the thickness contour map.

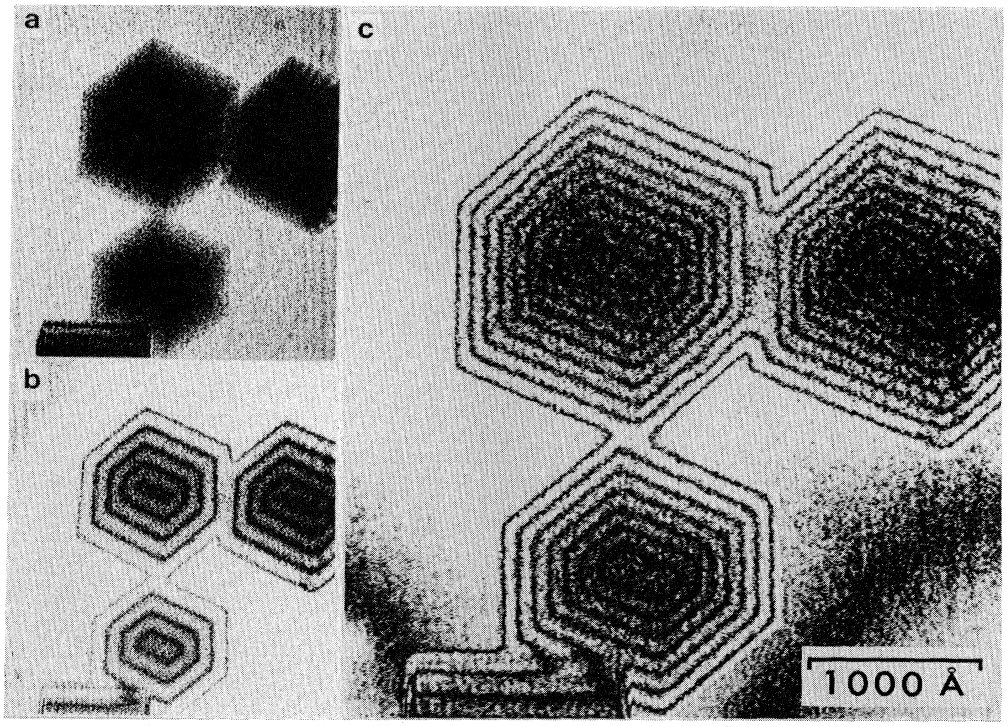

FIG. 33. Interference micrographs of magnesium-oxide particles: (a) reconstructed image; (b) interference micrograph; (c) two-times amplified interference micrograph. Although only the particle outlines can be seen in reconstructed image (a), the thickness distribution can also be observed in interference micrograph (b). Phase-amplified micrograph (c) reveals more detail thickness distribution.

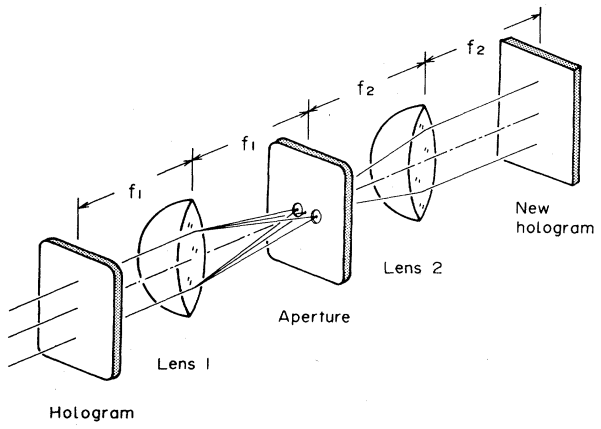

FIG. 34. Optical spatial filtering system for forming phase-amplified hologram.

A thickness change that causes a phase shift of 2π can be calculated as follows. Since its value is given by $(h/e)/(V_0/v)$, the thickness at an 80-kV accelerating voltage can be calculated to be between 200 and 600 Å by substituting $h/e = 4.1 \times 10^{-15}$ V s and $V_0 = 10-30$ V in the preceding formula. Measurement sensitivity is not so high, in spite of an extremely short wavelength for the electron beam. This is because the refractive index of the specimen is nearly equal to that of a vacuum.

2. Fine-particles example

An example for magnesium-oxide particles is shown in Fig. 33. The reconstructed image [Fig. 33(a)], which is equivalent to the electron micrograph, represents the intensity distribution of the transmitted electron beam. Information about the three-dimensional shape, other than the outlines of the particles, cannot be obtained.

Interference micrograph [Fig. 33(b)] looks three dimensional, since contour lines overlap on the electron micrograph in units of 500 Å thickness. The thickness can be observed at an arbitrary point in the electron micrograph. More detailed thickness distributions can be measured with a 2-times amplified interference micrograph [Fig. 33(c)], which is obtained using the optical reconstruction system shown in Fig. 28.

The minimum detectable phase difference in these interference micrographs is $\pi/4$, which corresponds to a thickness of ~ 60 Å. If the sensitivity is increased by more than 1 order of magnitude, measurement and observation are possible at atomic scales. In light optics, multiple-beam interferometry has already achieved a surprising sensitivity of 2.3 Å in thickness, which corresponds to a phase shift of $2\pi/2000$ (Sunagawa, 1961).

3. Phase-difference amplification

Recent results from Endo *et al.* (1984) and Tonomura, Matsuda, Kawasaki, Endo, and Osakabe (1985) mark the first step toward this dream. They applied an optical phase-difference amplification method to electron holography, as originally proposed by Bryngdahl (1969) and subsequently developed by Matsuda, Freund, and Hariharan (1981) for an optical field. With this method, a new hologram involving a 2-times phase amplification is formed using the optical spatial filtering system shown in Fig. 34. Amplification is achieved by selecting only the ±first-order diffracted beams using an aperture with two holes. This procedure is repeated, and the high amplification rate is obtained.

An example of a fine beryllium particle (Endo *et al.*, 1984) is shown in Fig. 35. A conventional interference

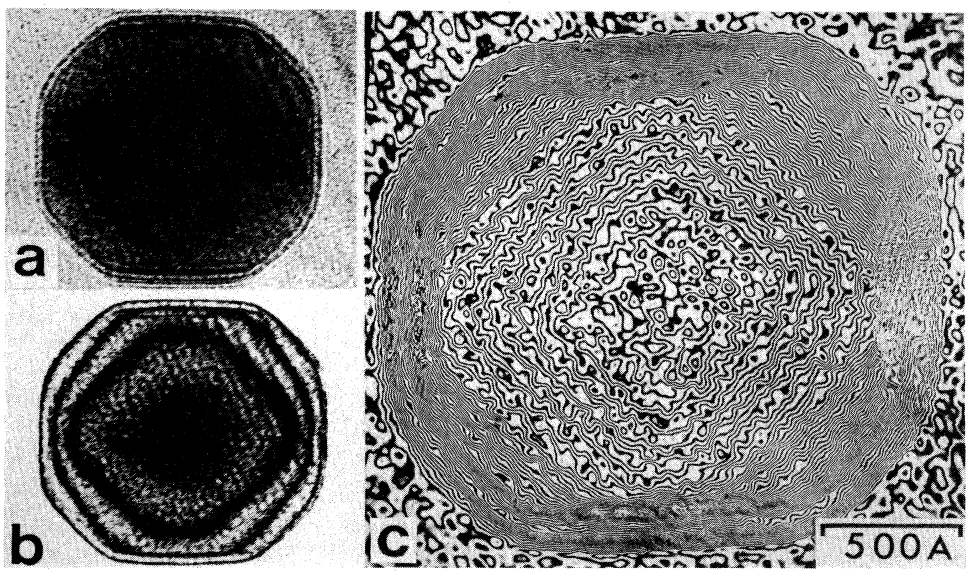

FIG. 35. Interference micrographs of a fine beryllium particle (Endo *et al.*, 1984): (a) reconstructed image; (b) interference micrograph; (c) 32-times amplified interference micrograph. Phase distribution was amplified 32 times, and a thickness contour map in units of only 13 Å was obtained.

micrograph [Fig. 35(b)] represents thickness contour lines in 440 Å units, while in a 32-times amplified interference micrograph [Fig. 35(c)], contour lines of units of only 13 Å can be observed. One may question whether these fringes represent the thickness distribution precisely, or whether they are only interpolations lacking any great degree of precision. This problem was examined through observation of surface steps (Tonomura, Matsuda, Kawasaki, Endo, and Osakabe, 1985) where the thickness change was already known.

Photographic evidence is shown in Fig. 36. The specimen is a molybdenite thin film approximately 50 Å in thickness. The phase shift can be observed as displacements of parallel interference fringes with equal spacings. The phase amplification rate is 24 times. Fringe steps can be recognized along lines designated A, B, and C in the photograph. These correspond to one, three, and five atomic steps on cleaved surfaces. The thickness change due to an atomic step is 6.2 Å, which is one-half of the c-axis lattice spacing and produces a phase shift of $2\pi/50$.

4. Future expectations

This technique is expected to have applications to biological and other fields. Biological specimens usually require staining or evaporation with heavy atoms before electron microscopic observation. This is because these specimens appear as phase objects to an illuminating electron beam, and contrast is hard to observe. However, if these specimens are to be observed at atomic scales, contrast should arise from the specimens themselves. Attached heavy atoms are only nuisances.

Since the phase shift of a 100-kV electron beam due to a single carbon atom has been calculated to be $2\pi/70$ (Cox and Bonham, 1967), phase contrast can be utilized for observation of biological specimens in electron microscopy just as in optical microscopy. Unstained biological specimens can thus be observed. The interference micrographs of an unstained ferritine molecule (Kawasaki *et al.*, 1986) shown in Fig. 37 encourage such a hope. The amplification rate in the interference micrograph is 24 times. Although the core of the ferritine molecule can be observed by conventional electron microscopy, the surrounding protein part can also be observed in these interference micrographs.

C. Observation of magnetic domain structures

1. Interpretation of contour maps

The magnetic domain structure of a ferromagnetic thin film has often been observed by Lorentz microscopy; black and white lines appear along magnetic domain walls with defocusing of an electron microscopic image. This is because the transmitted electrons are deflected in the direction determined by the magnetization in each domain. Although the principle behind this method can be explained by Lorentz force, the exact formulation should rely on wave optics, as investigated by Wohlleben (1966). Cohen (1967) further noted that holographic techniques could give direct information about the magnetic domain structures. It was subsequently demonstrated by Tonomura (1972) and Pozzi and Missiroli (1973) using electron interferometry that information about the domain structure was actually reflected in the electron phase distribution.

It was in 1980 that magnetic lines of force inside ferromagnetic particles were first actually observed as the contour fringes in interference micrographs (Tonomura,

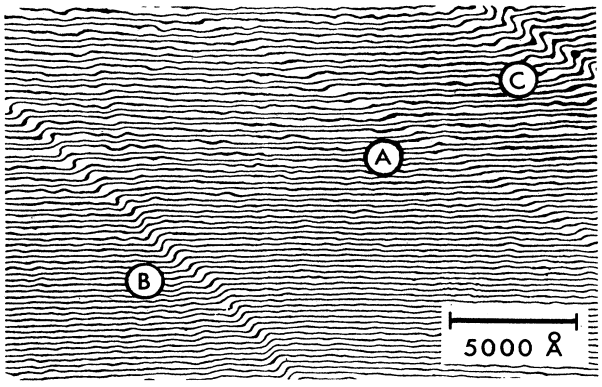

FIG. 36. Inteference micrograph of molybdenite thin film. (Tonomura, Matsuda, Kawasaki, Endo, and Osakabe, 1985): Atomic steps on cleaved surfaces of molybdenite thin film can be observed in a 24-times amplified interference micrograph. A monoatomic step is recognized along the line designated A, which corresponds to a thickness change of 6.2 Å and to an electron phase shift of $2\pi/50$.

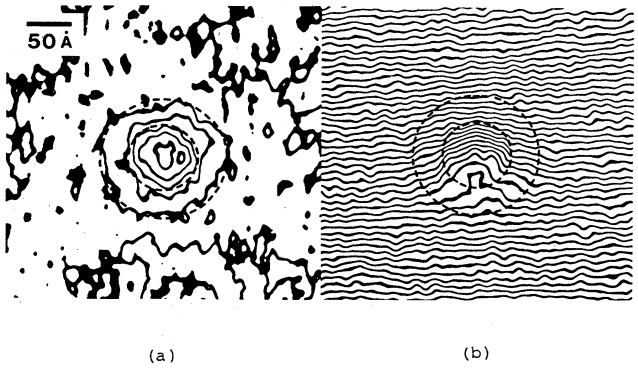

FIG. 37. Interference micrographs of an unstained ferritine molecule (Kawasaki *et al.*, 1986): (a) 24-times amplified interferogram; (b) 24-times amplified contour map. The surrounding protein part of the ferritine molecule, which is hardly seen in conventional electron microscopy, can be observed as well as the core.

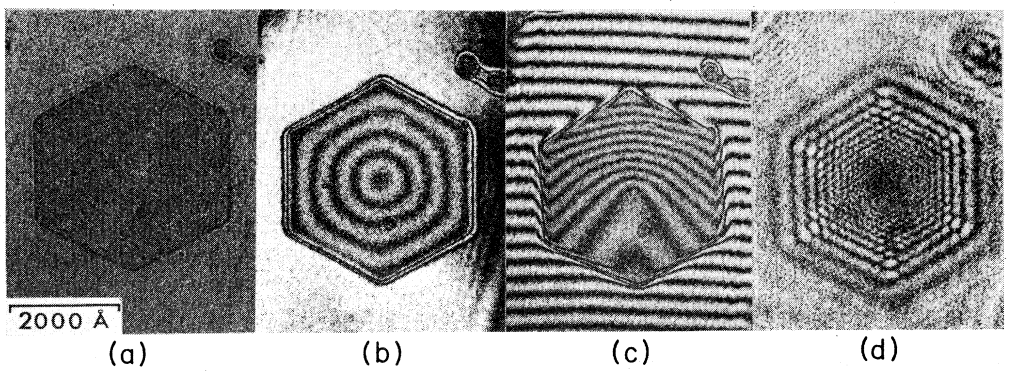

FIG. 38. Interference micrographs of a hexagonal fine cobalt particle: (a) reconstructed image; (b) two-times amplified contour map; (c) two-times amplified interferogram; (d) Lorentz micrograph. No contrast can be observed in reconstructed image (a), while in contour map (b) in-plane magnetic lines of force are displayed as contour fringes. The direction of magnetic line can be determined from interferogram (c) to be clockwise. Lorentz micrograph (d) can also be obtained optically from the same hologram, from which it is difficult to determine the magnetic domain structure.

Matsuda, Endo, Arii, and Mihama, 1980). This method has the following distinctive features compared with conventional Lorentz microscopy.[7]

(1) Intuitive interpretation is possible, since magnetic lines of force are drawn on an electron micrograph.

(2) Magnetic structures can be related to fine structures of a specimen, since there is no need to defocus an electron microscopic image.

(3) Quantitative measurement is possible, since a constant flux of h/e ($=4.1\times10^{-15}$ Wb) flows between two adjacent contour lines.

2. Example of ferromagnetic fine particles

An example of observation of magnetic lines of force is shown in Fig. 38. The specimen here is a plate-shaped cobalt fine particle. Reconstructed image [Fig. 38(a)], which is equivalent to the electron micrograph, has no contrast inside the particle image. This is because the thickness is uniform and the magnetization has no influence on the intensity of the transmitted electron beam. Information about the magnetization distribution is contained in the phase distribution.

In fact, concentric contour fringes appear in a 2-times phase-amplified interference micrograph [Fig. 38(b)]. Since the fringes can be directly interpreted as magnetic lines of force, it has become possible to observe how magnetic lines of force rotate in such a fine particle. Quantitative measurement is also possible, since a constant flux of $h/2e$ is contained between two adjacent contour lines.

Contour map [Fig. 38(b)] does not allow interpretation as to whether the magnetization direction is clockwise or counterclockwise. This, however, can be judged from interferogram [Fig. 38(c)], which is obtained by tilting two interfering beams slightly in the optical reconstruction stage. The wave front of the transmitted electron beam is first retarded at the particle edge due to the thickness effect. Then it is conversely advanced inside the particle due to the magnetic effect. This means the magnetization is clockwise. If the particle surface is turned over, the rotation direction becomes counterclockwise and consequently the wave front is retarded at the particle center.

It has been very difficult to determine experimentally the magnetization distribution in such a fine particle. Even when observed by Lorentz microscopy, which provides magnetic domain structure information with the highest spatial resolution currently available, the magnetic structure is difficult to identify. This is because the magnetic contrast overlaps with the diffraction pattern of the particle due to the large defocusing necessary for domain structure observation. A Lorentz micrograph of the particle is shown in Fig. 38(d). This was obtained optically from the same electron hologram, something that is possible because a hologram contains all the information on the scattered electron wave from an object. Consequently a Lorentz micrograph can also be optically obtained from the hologram merely by defocusing the reconstructed image. Since the outer shape of the particle is completely blurred in Lorentz micrograph [Fig. 38(d)], it is not easy to predict the magnetization distribution.

An interference micrograph of a triangular cobalt particle is also shown in Fig. 39(a). Since the particle shape is that of a triangular pyramid truncated parallel to the base plane, as shown in Fig 39(b), two kinds of interference fringes can be observed in the interference micro-

[7]Electron interference microscopy of magnetic specimens such as ferromagnetic thin film, a magnetic monopole, and a toroidal ferromagnet was theoretically investigated by Fukuhara *et al.* (1983). Applications to the observation of magnetic domain structure were reported by Tonomura *et al.* (1982b). Theoretical predictions were also made by Wahl and Lau (1979) that contour lines would follow magnetic lines of force.

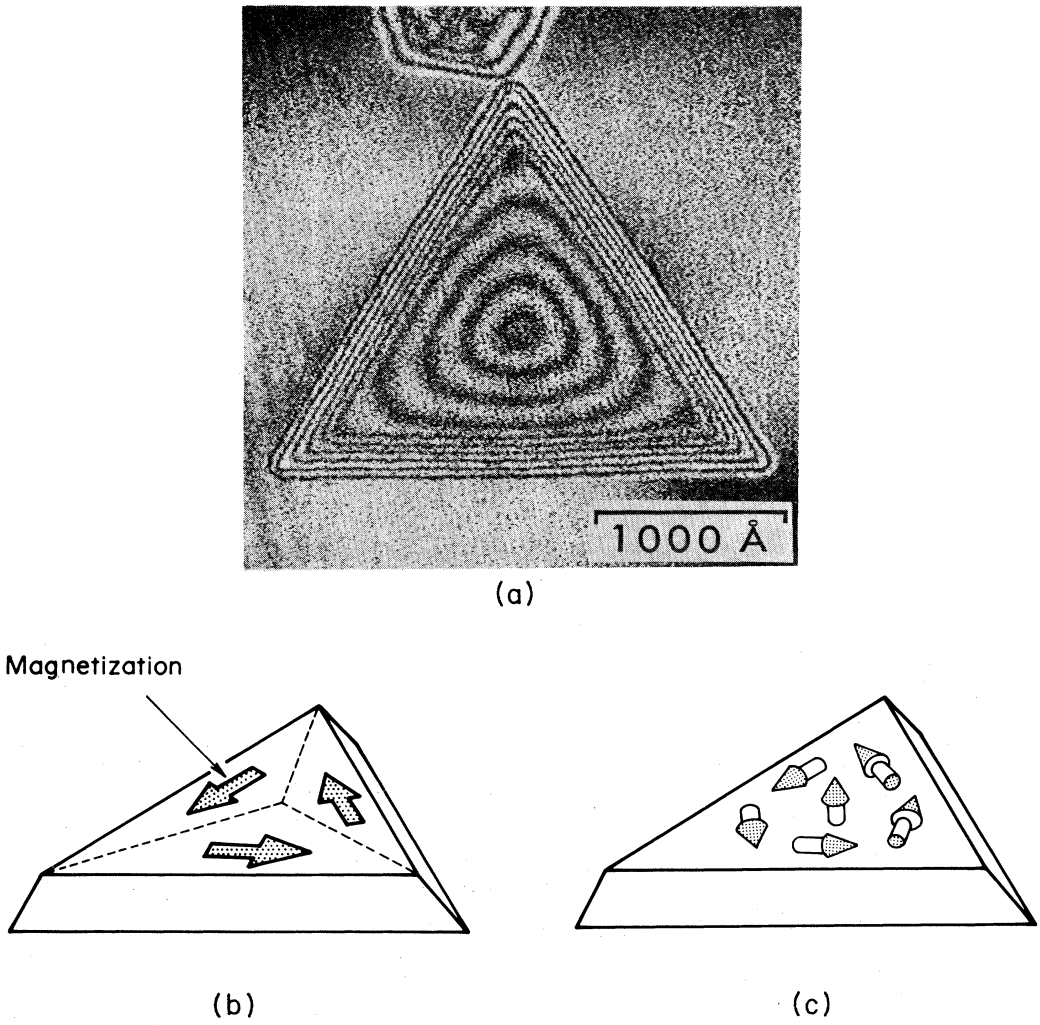

FIG. 39. Interference micrograph of triangular cobalt fine particle (Tonomura, Matsuda, Endo, Arii, and Mihama, 1980): (a) two-times amplified interference micrograph; (b) domain structure; (c) magnetization configuration near the particle center. The peripheral contour fringes in interference micrograph (a) indicate the thickness contour lines, and the inner fringes indicate magnetic lines of force. The detailed examination of the wave front clarified that the magnetization stands up in the central region of the particle 150 Å in radius.

graph. Contour fringes parallel to the three edges show that the thickness increases to 550 Å from the edges. The inner contour fringes indicate magnetic lines of force, since thickness is uniform there.

Although the observed magnetization distribution can be thoroughly explained in theoretical terms, a question arises concerning the magnetization distribution at the center of the triangular particle. It is not reasonable to expect that the magnetization rotates even in the extreme center, since the magnetization would have to rotate very rapidly there and consequently the exchange energy would have to diverge. This problem was solved by measuring details of the wave front at the particle center from the microarea low-angle electron diffraction patterns obtained from the electron hologram in the optical reconstruction stage (Tonomura and Matsuda, 1980; Tonomura, Matsuda, Endo, Arii, and Mihama, 1980).

The reason for utilizing electron diffraction is that it is more purely quantitative than mere observation of the wave front as a contour map. The results prove that the magnetization stands up perpendicular to the base plane in the particle center; the area where the magnetization stands up is approximately 150 Å in radius [see Fig. 38(c)].

3. Example of cross-tie wall

A case is shown in Fig. 40 in which even a complex magnetic domain structure can be easily determined using interference electron microscopy. Since magnetic lines of force can be observed with this technique, such a complex magnetization distribution near a cross-tie wall can be

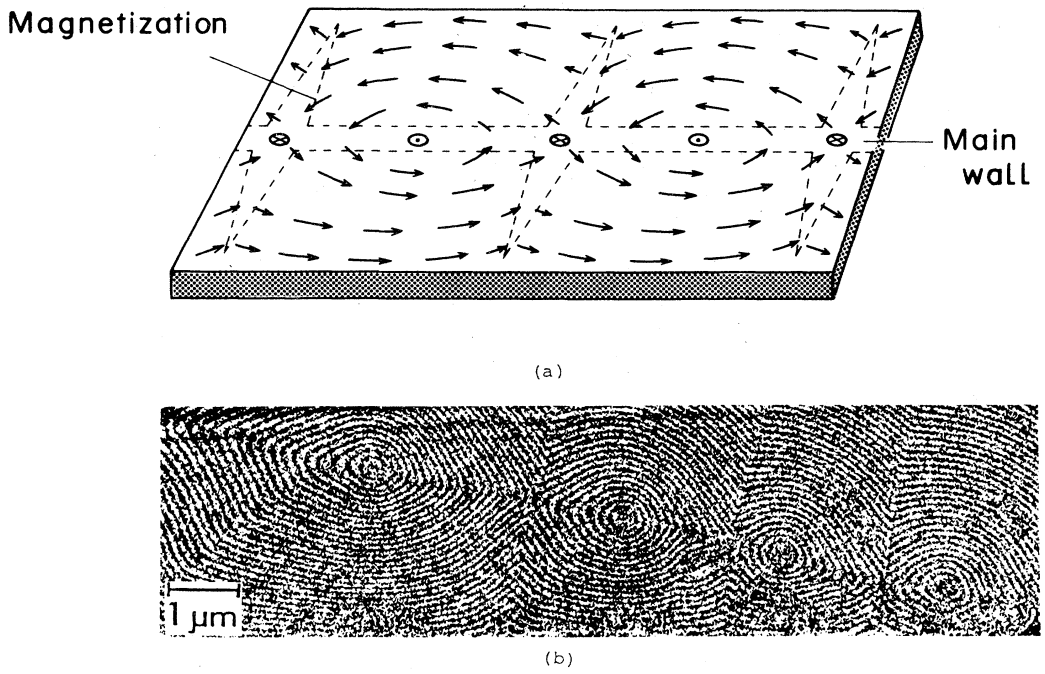

FIG. 40. Cross-tie wall in Permalloy thin film: (a) predicted magnetization distributions; (b) interference micrograph.

directly observed. Magnetic lines of force, obtained by connecting the magnetization arrows in predicted magnetization model [Fig. 40(a)], are actually visualized by interference micrograph [Fig. 40(b)]. It can also be deduced from the micrograph that the magnetization stands up perpendicular to the film plane at mountain tops and saddle points of the electron wave front. This is because the incident wave front traverses the film without any disturbance from the magnetization.

D. Measurement of magnetic field distributions

A constant magnetic flux is contained between two adjacent contour lines in interference micrographs; thus quantitative observation is possible of magnetic fields distributed in space (Matsuda *et al.*, 1982), which have previously been inaccessible using conventional Lorentz microscopy.[8] One example is that of high-density magnetic recording (Osakabe *et al.*, 1983; Yoshida *et al.*, 1983).

[8]A defocused mode in Lorentz microscopy allows observation only of magnetic fields having directions or magnitudes that change suddenly, as at a magnetic domain wall. More precisely, the contrast in a Lorentz micrograph can be interpreted by a purely imaginary term added to Eq. (27). The value of this term vanishes when the condition curl $B=0$ is satisfied, as in the case of magnetic fields in space. However, magnetic fields were observed with a Foucault mode in Lorentz microscopy by Jakubovics (1964). Stray magnetic fields have recently been measured with a new technique of differential phase-contrast imaging by McFadyen, Chapman, and McVitie (1985).

1. Application to high-density magnetic recording

Magnetic recording plays an important role in the storage of information for a variety of applications from consumer goods to computer memories. With steady increases in information quantity, recording densities keep on rising every year. The recording bit length is accordingly threatening to break past the 1-μm barrier. When considering such a situation, detailed observations of recorded magnetization patterns are required, since recording density is moving toward fundamental limitations.

An interference micrograph of a recorded cobalt film is shown in Fig. 41. Magnetic recording was carried out using a moving magnetic head [Fig. 41(a)]. The film covers only the lower part of the micrograph [Fig. 41(b)] and is observed from above. The upper part is free space. Arrows in the micrograph indicate the directions of the recorded magnetization. Recorded magnetic lines of force can be observed as contour fringes along arrows. At the boundaries between two opposing magnetizations, magnetic lines of force behave like vortices. As they approach the film edge they meander. Finally, they leak outside into space. The leakage flux can be quantitatively measured in the micrograph.

In order to achieve higher-density recording, the width of the transition region has first to be made small. This width depends greatly on the magnetic characteristics of the film materials, and also on the recording method. With observation by interference microscopy, a bit length of 0.15 μm could be demonstrated by adjusting experimental conditions. The resultant interference micrograph

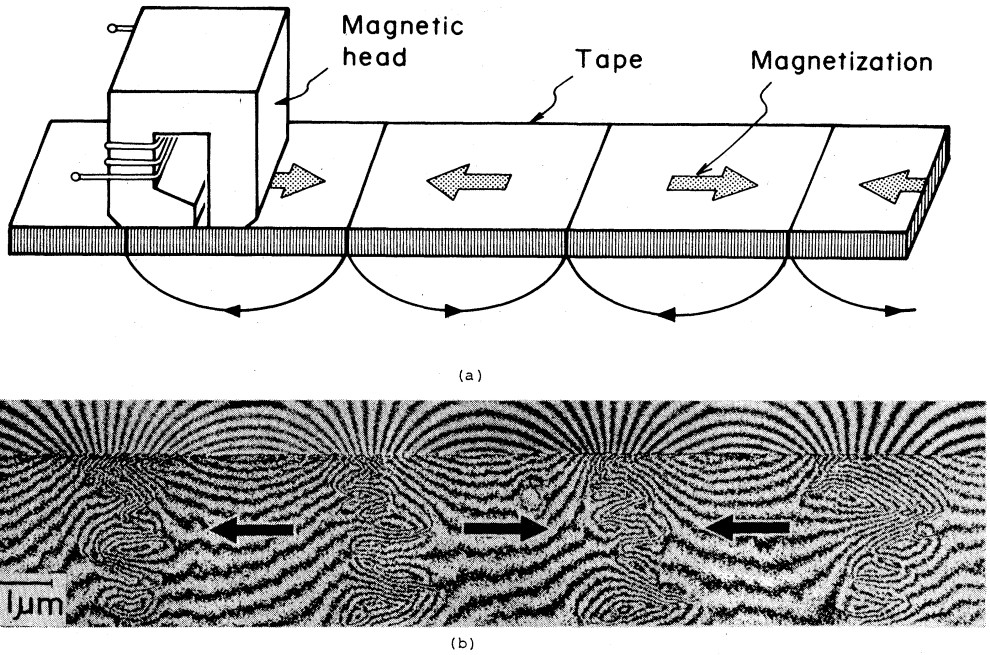

FIG. 41. Recorded magnetization pattern in cobalt magnetic tape: (a) schematic of recording method; (b) two-times amplified interference micrograph.

phase-amplified 10 times is shown in Fig. 42. Only magnetic lines of force leaking outside the recorded film can be observed.

2. Magnetic monopoles

Observation of magnetic monopoles also needs to be discussed (Fukuhara *et al.*, 1983), since this will throw additional light on certain essential features of electron interaction with electromagnetic fields. A candidate event for monopole detection reported in 1982 involved use of a superconducting flux meter known as SQUID (Cabrera, 1982). No events have since then been detected, although many trials are known to have taken place.

The measuring principle of SQUID is very similar to that of interference electron microscopy. Interference phenomena of Cooper pairs in a superconductor are utilized for measurement. Consequently magnetic flux can be measured in $h/2e$ units instead of the h/e units used with electron interference, since a Cooper pair has an electric charge of $2e$. This magnetic flux measurement can be observed to be the most direct means of monopole detection.

FIG. 42. Ten-times amplified interference micrograph of recorded cobalt magnetic tape (bit length, 0.15 μm). Only leakage fluxes can be observed.

If a monopole is trapped in, for example, a ferromagnet, interference electron microscopy may also be used for its detection. The wave front of an electron beam incident on a monopole with magnetic charge g is considered in Fig. 43. The wave front is rotated on an axis determined by a magnetic line of force; more exactly, a phase difference is produced proportional to the magnetic flux enclosed by two beams, as given by Eq. (27). In this case, the transmitted wave front can be determined easily. Since magnetic lines of force from a monopole are radial, the transmitted wave front rises while moving around it. The resultant wave front is something like a spiral staircase. The position arrived at after one round is not the original one, but one on the second floor of the wave front. There are infinite floors.

Such strange behavior by the wave front can be clearly understood only if the magnetic charge satisfies the Dirac quantization condition $g=n(h/e)$. The phase difference in wave-front height between two adjacent floors is equal to an integral multiple (n) of 2π. Consequently contour lines of the wave front become the same for all floors.

E. Measurement of hidden magnetic flux through vector potentials

1. Significance of potentials—the Aharonov-Bohm effect

Electromagnetism is classically represented by electric and magnetic fields, which are defined by the forces act-

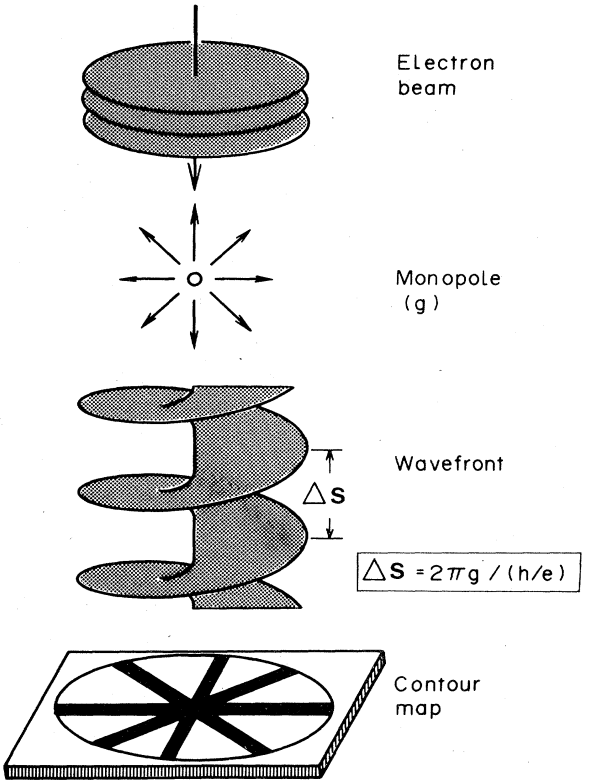

FIG. 43. Electron wave front incident on monopole.

ing on an electron. In quantum mechanics, interaction between electrons and an electromagnetic field is specified by potentials. These potentials, in turn, give rise to phase shifts in the electron wave function.

Potentials were once regarded as a mathematical convenience and interpreted as having no physical significance. There is some question today whether they are a fact or not in a quantum mechanics context. One very important effect bearing on this question was clarified by Aharonov and Bohm (1959). The Aharonov-Bohm (AB) effect demonstrates the fact that an electron beam is physically influenced while passing through a space in which there are no fields but only potentials.

The AB effect in a magnetic case is illustrated in Fig. 44. A magnetic field is produced only inside an infinite solenoid by applying an electric current to it. Two coherent electron beams from a point source pass on both sides of the solenoid, and are overlapped to measure the phase difference as an interference pattern. A phase difference proportional to the magnetic flux inside the solenoid is then produced between the two beams in addition to the path difference, as can easily be deduced from Eq. (27).

It seems strange from the classical point of view that an observable effect is produced for an electron beam passing through field-free regions, and consequently receiving no forces. However, the direct consequence [Eq. (27)] from the Schrödinger equation, that a phase shift is

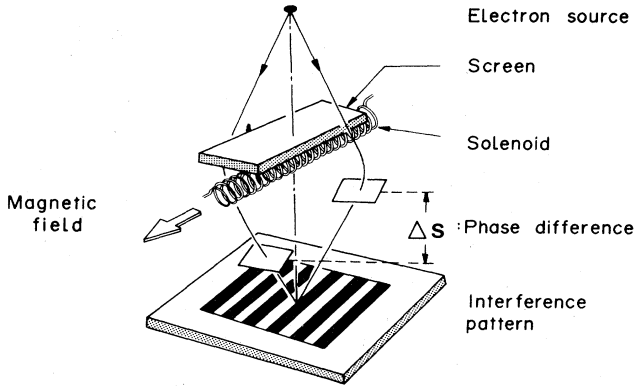

FIG. 44. Aharonov-Bohm effect. A phase difference proportional to the magnetic flux is produced between two electron beams passing on both sides of the solenoid, even if they do not touch the magnetic field.

proportional to $\oint \mathbf{A}\,ds$, points unavoidably to the conclusion that a phase shift is produced by vector potential **A** along electron paths, irrespective of the existence of magnetic field **B**. An electron couples directly with the vector potential, and not with the magnetic fields.

The significance of this effect has recently taken on weight, since the AB effect has been regarded as an explicit manifestation of the validity of the gauge principle in electromagnetism (Wu and Yang, 1975). Although the existence of this effect was experimentally tested by several authors shortly after its prediction (Chambers, 1960; Boersch *et al.*, 1961; Fowler *et al.*, 1961; Möllenstedt and Bayh, 1962), it was questioned by Bocchieri and Loinger (1978) on both theoretical and experimental grounds. They described the effect as being of purely mathematical origin. Earlier experiments were also questioned by Roy (1980); as he explained it, the measured phase shifts might have been due to inevitable leakage flux from finite whiskers or solenoids used in the experiments. Since then, the controversy has flared up mainly in theoretical circles.

An electron interference experiment was carried out by Tonomura *et al.* (1982a) that removed ambiguity regarding leakage flux with the help of electron holography. A tiny ferromagnetic sample was fabricated, which had a toroidal geometry and formed a completed magnetic circuit without leakage flux. An electron beam was made incident on the sample, and the phase difference between two beams passing through spaces inside the hole and outside the sample was measured. The resultant interference patterns is shown in Fig. 45(b), where the phase distribution is observed as a shift of regular fringes. The fringes inside and outside the toroid are displaced by six fringes, thus indicating the existence of the AB effect. It was clarified by holographic interference microscopy that the amount of leakage flux from the toroid was too small to disturb the result, as can be seen in the interference micrograph in Fig. 46. The leakage flux problem was also tested by Möllenstedt, Schmid, and Lichte (1982), who

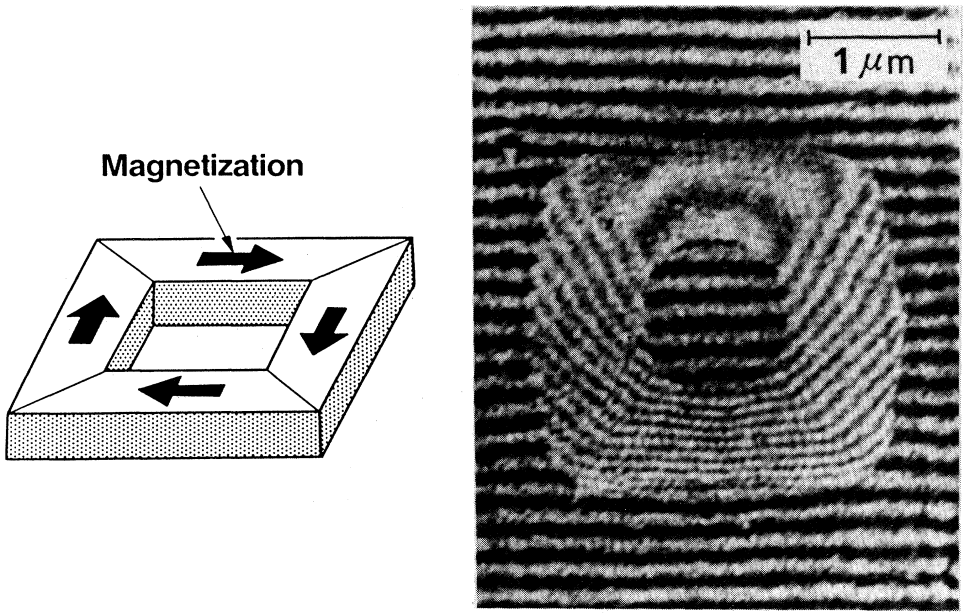

FIG. 45. Experiment to confirm the AB effect (Tonomura *et al.*, 1982a) (a) schematic of toroidal magnet; (b) interferogram. Instead of a solenoid, a ferromagnet with toroidal geometry was employed for the experiment to remove fringing fields. The resultant interferogram (b) indicates that a phase shift of six wavelengths exists between two beams passing through spaces inside the hole and outside the toroid.

reached the same conclusion.

This experiment was disputed by Bocchieri, Loinger, and Siragusa (1982). They felt that the observed phase difference was not due to the AB effect, but to the Lorentz force effect of electrons penetrating into the ferromagnet. To test this, an experiment was performed by Tonomura, Umezaki, Matsuda, Osakabe, Endo, and Sugita (1984) with a toroidal ferromagnet having a top surface covered with a gold layer to prevent electron penetration. Still, the results remained the same.

2. Observation of the flux quantization process—Experimental proof of the Aharonov-Bohm effect

The AB effect assures that even a magnetic flux completely hidden from an electron beam can be detected by the beam due to local interaction with vector potentials. This face was utilized in a recent experiment by Tonomura, Osakabe, Matsuda, Kawasaki, Endo, Yano, and Yamada (1986) in which the process of magnetic flux quantization in a superconductor[9] was directly observed by electron interferometry. This experiment also confirmed the AB effect under conditions where any overlap be-

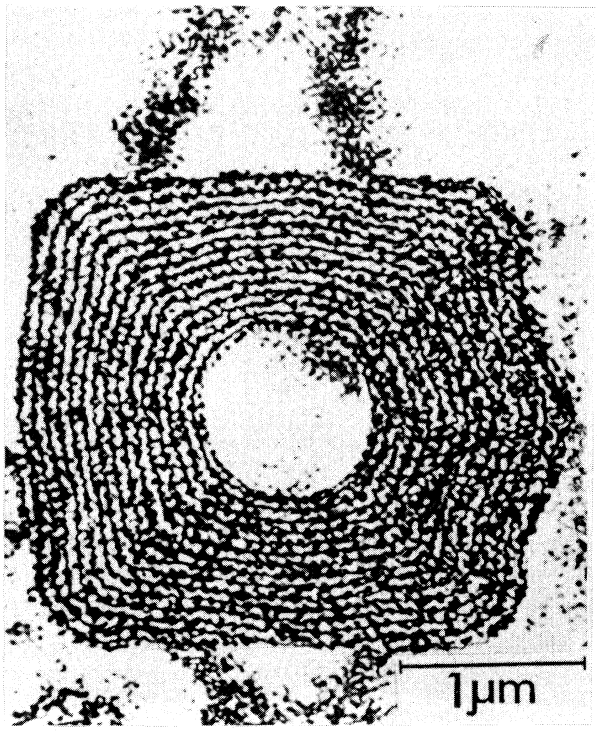

FIG. 46. Two-times amplified interference micrograph of toroidal magnet. Since contour fringes indicate magnetic flux in $h/2e$ units, only $\frac{1}{15}$ of the total flux, i.e., a flux of $h/2e$ is leaking outside the toroidal, which is too small to explain the observed phase shift in Fig. 45(b).

[9]Quantized magnetic flux in a superconductor has been observed by interference electron microscopy. See Lischke (1969); Wahl (1970). Details of the experiment by Tonomura *et al.* (1986) can be found in a paper by Osakabe *et al.* (1986).

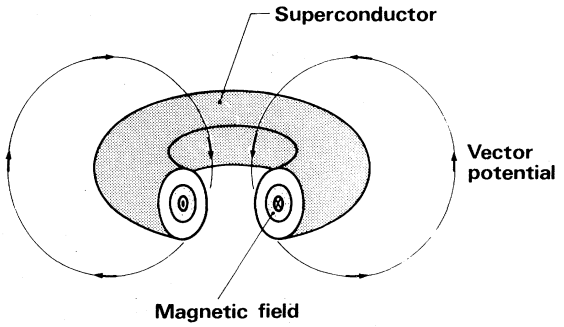

FIG. 47. Schematic of toroidal magnet completely covered with superconductor layer.

tween an electron beam and magnetic fields was exceedingly small, as had been demanded by Bocchieri, Loinger and Siragusa (1982).

The specimen employed in this experiment was a toroidal ferromagnet completely covered with a niobium layer, as shown in Fig. 47. A magnetic field rotates inside the toroid to form a completed circuit. This was tested by interference electron microscopy. When an electron beam is incident on a sample, it interacts with the vector potential outside the sample. A phase shift is then produced between the two parts passing through the hole and outside the toroid The interference pattern obtained in this case is different from that shown in Fig. 45 in one major way. The fringes cannot be observed inside the toroid, since it is impenetrable. Consequently, only a modulo nh/e can be measured.

The interference pattern was examined when the specimen was cooled below the superconducting critical temperature of Nb, 9.2 K. A dramatic change occurs inside the Nb layer when the specimen temperature crosses the critical temperature, which can be observed through interaction of the electron beam with the vector potential. Electrons in the superconductor form Cooper pairs, which, in phase, form a coherent wave. In order for the coherent wave encircling the magnetic field to persist, the phase of the wave turning around the magnetic field has to be the same modulo 2π as the original value. Otherwise, the superconducting state will break down.

Since a Cooper pair has a mass of $2m$ and an electric charge of $2e$, the phase difference is given by twice the value of the electron beam:

$$\Delta S=\frac{1}{\hbar}\oint(2m\mathbf{v}-2e\mathbf{A})d\mathbf{s}\ . \tag{28}$$

The value ΔS integrated along a closed path around the magnetic field has to be a precise integral multiple of 2π, i.e., $2n\pi$. The circumstances are extremely simple if the magnetic flux is an integral multiple of $h/2e$. In this case, the phase condition can be automatically satisfied without any change in the superconducting state.

In the case of a general magnetic flux, Cooper pairs have to have momenta such that the phase difference ΔS may be equal to $2n\pi$. That is, a supercurrent flows around the magnetic field to form a quantized magnetic flux in $h/2e$ units by adding the magnetic field produced

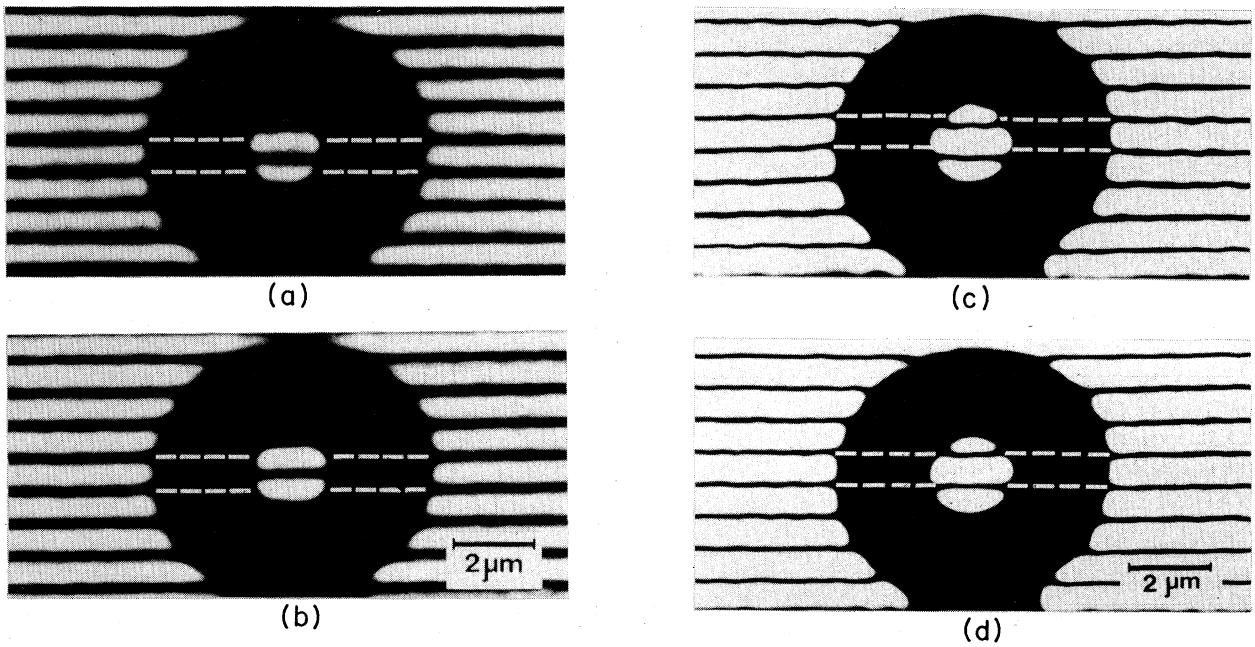

FIG. 48. Interferograms showing phase distribution inside the hole and outside the toroid: (a) interferogram at $T=15$ K; (b) interferogram at $T=4.5$ K; (c) two-times amplified interferogram at $T=15$ K; (d) two-times amplified interferogram at $T=4.5$ K. Interference fringes were displaced by 0.4 fringe spacing between the inside of the hole and the outside of the toroid at 15 K (a). The fringe displacement suddenly changed to just half a spacing (b) when the specimen temperature crossed the critical temperature 9.2 K. This change can be seen clearly in phase-amplified interferograms (c) and (d).

by the supercurrent. Such a physical change inside the superconductor can be visualized by electron interferometry.

A specimen in this experiment was fabricated by photolithography and observed by interference electron microscopy while cooling down. Resultant interference fringes are shown in Figs. 48(a) and 48(b). The fringes inside the hole and outside the toroid suddenly moved, to be displaced by just half a fringe spacing, when the specimen temperature crossed by the critical temperature. This can more easily be seen from the 2-times phase-amplified interference micrographs shown in Figs. 48(c) and 48(d). This case corresponds to the trapping of an odd number of flux quanta within the superconductor. Of course, an even number of flux quanta could also be observed for toroidal samples with different magnetic fluxes where no phase difference was detected.

These experimental results indicate that direct observation of the quantization process of the magnetic flux in a superconductor is possible as a result of the interaction of an electron beam with the surrounding vector potential. In addition, decisive evidence was provided of the validity of the AB effect.[10] Overlap between magnetic fields and the electron beam was in this case extremely small; leakage fields from the toroidal magnet were shielded by the Meissner effect of the surrounding superconductor. Furthermore, the electron beam was prevented from penetrating into the magnet.

CONCLUSIONS AND FUTURE PROSPECTS

It could be said that electron interferometry was born with the invention of the electron biprism in 1954. This technique provides possibilities for both measurement and observation at the atomic level, due to the extremely short wavelength of an electron beam. However, the technique has not yet become widespread due to the fact that delicate and elaborate techniques are required. Consequently only a limited number of interesting experiments have yet been reported.

Recently this technique has been given a major boost by the development of a coherent electron beam. Electron interference fringes have not only become easily observable with a field-emission electron beam that can produce as many as 3000 interference fringes, but new areas of electron interferometry have also been opened by the introduction of electron holography. In addition, electron interferometry has been demonstrated to be applicable in such fields of fundamental physics as confirmation of the AB effect and magnetic flux quantization. These effects are shown particularly vividly because the phase distribution of an electron wave function is displayed before the researcher's very eyes.

Electron interferometry has also made remarkable progress in measurement precision via the use of phase amplification techniques, something peculiar to holography. As of this writing, a phase shift as small as $2\pi/50$ has become measurable; with this technique even a thickness change of only a monoatomic step has been detected.

This recent progress has given rise to expectations that electron interferometry will become a useful tool for investigating the microscopic world. A variety of exciting applications promise to open up in fields ranging from basic physics to practical technologies.

Note added in proof. A high resolution image reconstruction has recently been reported by Lichte (1986).

ACKNOWLEDGMENTS

I should like to thank Junji Endo, Shuji Hasegawa, Takeshi Kawasaki, Tsuyoshi Matsuda, and Nobuyuki Osakabe, my collaborators at Hitachi's Advanced Research Laboratory, who worked on development of the apparatus and experiments on electron holography. Thanks are also due to Professor Tatsuo Arii of the National Institute of Physiological Sciences, Professor Kazuhiro Mihama of Nagoya University, Dr. Akira Fukuhara, Dr. Yutaka Sugita, and Dr. Ushio Kawabe of Hitachi, Ltd., and Dr. Hideo Fujiwara of Hitachi Maxell, Ldt. for their cooperation and helpful discussions during our work on electron holography. My sincere gratitude also goes to Professor Chen Ning Yang of SUNY Stony Brook for new ideas regarding electron interference experiments, and to Professor Emeritus Ryoji Uyeda of Nagoya University for his helpful and stimulating discussions. Lastly, I am grateful to Professor Mark P. Silverman, at present a visiting senior researcher in our laboratory, for his comments during the preparation of this paper.

REFERENCES

Aharonov, Y., and D. Bohm, 1959, Phys. Rev. **115**, 485.
Baez, A. V., 1952, J. Opt. Soc. Am. **42**, 756.
Bocchieri, P., and A. Loinger, 1978, Nuovo Cimento A **47**, 47.
Bocchieri, P., A. Loinger, and G. Siragusa, 1982, Lett. Nuovo Cimento **35**, 370.
Boersch, H., 1940, Naturwissenschaften **28**, 711.
Boersch, H., 1954, Z. Phys. **139**, 115.
Boersch, H., 1960, Z. Phys. **159**, 397.
Boersch, H., H. Hamisch, K. Grohman, and D. Wohlleben, 1961, Z. Phys. **165**, 79.
Bonnet, M., M. Troyon, and P. Gallion, 1978, in *Proceedings of the 9th International Congress in Electron Microscopy,* Toronto, edited by J. M. Sturgess (Microscopical Society of Canada, Toronto), Vol. 1, p. 222.
Bryngdahl, O., 1969, J. Opt. Soc. Am. **59**, 142.
Busch, H., 1926, Ann. Phys. (Leipzig) **81**, 974.
Cabrera, B., 1982, Phys. Rev. Lett. **48**, 1378.
Chambers, R. G., 1960, Phys. Rev. Lett. **5**, 3.
Cohen, M. S., 1967, J. Appl. Phys. **38**, 4966.
Cox, H. L., Jr., and R. A. Bonham, 1967, J. Chem. Phys. **47**,

[10]An experiment concerning the existence of the AB effect in superconductors has recently been reported by Walker (1986).

2599.
Crewe, A. V., D. N. Eggenberger, D. N. Wall, and L. N. Welter, 1968, Rev. Sci. Instrum. **39**, 576.
Crewe, A. V., J. Wall, and J. Langmore, 1970, Science **168**, 1338.
DeVelis, J. B., G. B. Parrent, and B. J. Thompson, 1966, J. Opt. Soc. Am. **56**, 423.
Ehrenberg, W., and R. E. Siday, 1949, Proc. Phys. Soc. London, Sec. B **62**, 8.
Endo, J., T. Kawasaki, T. Matsuda, N. Osakabe, and A. Tonomura, 1984, in *Proceedings of the 13th International Commission for Optics,* edited by H. Ohzu (Organizing Committee of ICO-13, Sapporo, 1984), p. 480.
Endo, J., T. Matsuda, and A. Tonomura, 1979, Jpn. J. Appl. Phys. **18**, 2291.
Fowler, L. H., L. Marton, J. A. Simpson, and J. A. Suddeth, 1961, J. Appl. Phys. **32**, 1153.
Frabboni, S., G. Matteucci, and G. Pozzi, 1985, Phys. Rev. Lett. **55**, 2196.
Fukuhara, A., K. Shinagawa, A. Tonomura, and H. Fujiwara, 1983, Phys. Rev. B **27**, 1839.
Gabor, D., 1949, Proc. R. Soc. London, Ser. A **197**, 454.
Gabor, D., 1951, Proc. Phys. Soc. London, Sec. B **64**, 449.
Gingras, Y., 1980, Am. J. Phys. **48**, 84.
Haine, M. E., and J. Dyson, 1950, Nature (London) **166**, 315.
Haine, M. E., and T. Mulvey, 1952, J. Opt. Soc. Am. **42**, 763.
Hanszen, K.-J., 1970, Optik **32**, 74.
Hanszen, K.-J., 1982, in *Advances in Electronics and Electron Physics,* edited by L. Marton (Academic, New York), Vol. 59, p. 1.
Hibi, T., 1956, J. Electron Microsc. **4**, 10.
Jakubovics, J. P., 1964, Philos. Mag. **10**, 675.
Kawasaki, T., J. Endo, T. Matsuda, N. Osakabe, and A. Tonomura, 1986, J. Electron Microsc. **35**, 211.
Kirkpatrick, P., and H. M. A. El-Sum, 1956, J. Opt. Soc. Am. **46**, 825.
Klein, A. G., and S. A. Werner, 1983, Rep. Prog. Phys. **46**, 259.
Konopinski, K. J., 1978, Am. J. Phys. **46**, 499.
Krimmel, E., 1960, Z. Phys. **158**, 35.
Kulyupin, Yu A., S. A. Nepijko, N. N. Sedov, and V. G. Shamonya, 1978, Optik **52**, 101.
Lauer, R., 1984, Optik **67**, 159.
Leith, E. N., and J. Upatnieks, 1962, J. Opt. Soc. Am. **52**, 1123.
Lenz, F., and G. Wohland, 1984, Optik **67**, 315.
Lichte, H., 1982, in *Proceedings of the 10th International Congress on Electron Microscopy,* Hamburg, edited by the Congress Organizing Committee (Deutsche Gesellschaft für Elektronenmikroskopie, Frankfurt), Vol. 1, p. 411.
Lichte, H., 1985, Optik **70**, 176.
Lichte, H., 1986, Ultramicroscopy **20**, 293.
Lischke, B., 1969, Phys. Rev. Lett. **22**, 1366.
Marton, L., 1952, Phys. Rev. **85**, 1057.
Matsuda, K., C. H. Freund, and P. Hariharan, 1981, Appl. Opt. **20**, 2763.
Matsuda, T., A. Tonomura, R. Suzuki, J. Endo, N. Osakabe, H. Umezaki, H. Tanabe, Y. Sugita, and H. Fujiwara, 1982, J. Appl. Phys. **53**, 5444.
Matsumoto, K., and M. Takahashi, 1970, J. Opt. Soc. Am. **60**, 30.
Matteucci, G., G. F. Missiroli, and G. Pozzi, 1982, Ultramicroscopy **8**, 403.
McFadyen, I. R., J. N. Chapman, and S. McVitie, 1985, in Proceedings of the 11th International Colloquium on Magnetic Films and Surfaces, Asilomar State Park, California.
Meier, R., 1965, J. Opt. Soc. Am. **55**, 987.
Merli, P. G., G. F. Missiroli, and G. Pozzi, 1974, J. Microsc. (Paris) **21**, 11.
Missiroli, G. F., G. Pozzi, and U. Valdrè, 1981, J. Phys. E **14**, 649.
Mitsuishi, T., H. Nagasaki, and R. Uyeda, 1951, Proc. Jpn. Acad. **27**, 86.
Möllenstedt, G., and W. Bayh, 1962, Phys. Bl. **18**, 299.
Möllenstedt, G., and H. Dücker, 1955, Naturwissenschaften **42**, 41.
Möllenstedt, G., H. Schmid, and H. Lichte, 1982, in *Proceedings of the 10th International Congress on Electron Microscopy,* edited by the Congress Organizing Committee (Deutsche Gesellschaft für Elektronenmikroskopie, Frankfurt), p. 433.
Möllenstedt, G., and H. Wahl, 1968, Naturwissenschaften **55**, 340.
Müller, E. W., 1937, Z. Phys. **106**, 541.
Munch, J., 1975, Optik **43**, 79.
Osakabe, N., T. Matsuda, T. Kawasaki, J. Endo, A. Tonomura, S. Yano, and H. Yamada, 1986, Phys. Rev. A **34**, 815.
Osakabe, N., K. Yoshida, Y. Horiuchi, T. Matsuda, H. Tanabe, T. Okuwaki, J. Endo, H. Fujiwara, and A. Tonomura, 1983, Appl. Phys. Lett. **42**, 746.
Pozzi, G., and G. F. Missiroli, 1973, J. Microsc. (Paris) **18**, 103.
Rogers, G. L., 1951, Proc. R. Soc. Edinburgh, Sect. A **63**, 193.
Rogers, J., 1980, in *Advances in Optical and Electron Microscopy,* edited by M. Schlenker, M. Fink, J. P. Goedgebeur, C. Malgrange, J. Ch. Vlénot, and R. H. Wade (Springer, Berlin), Vol. 8, p. 365.
Roy, S. M., 1980, Phys. Rev. Lett. **44**, 111.
Saxon, G., 1972, Optik **35**, 195.
Silverman, 1986, Phys. Lett. A **118**, 155.
Sunagawa, I., 1961, Am. Mineral. **46**, 1216.
Tomita, T., T. Matsuda, and T. Komoda, 1970, Jpn. J. Appl. Phys. **9**, 719.
Tomita, T., T. Matsuda, and T. Komoda, 1972, Jpn. J. Appl. Phys. **11**, 143.
Tonomura, A., 1969, J. Electron Microsc. **18**, 77.
Tonomura, A., 1972, Jpn. J. Appl. Phys. **11**, 493.
Tonomura, A., A. Fukuhara, H. Watanabe, and T. Komoda, 1968, Jpn. J. Appl. Phys. **7**, 295.
Tonomura, A., and T. Matsuda, 1980, Jpn. J. Appl. Phys. **19**, 97.
Tonomura, A., T. Matsuda, and J. Endo, 1979, Jpn. J. Appl. Phys. **18**, 9.
Tonomura, A., T. Matsuda, T. Endo, J. Arii, and K. Mihama, 1980, Phys. Rev. Lett. **44**, 1430.
Tonomura, A., T. Matsuda, J. Endo, T. Arii, and K. Mihama, 1986, Phys. Rev. B **34**, 3397.
Tonomura, A., T. Matsuda, J. Endo, H. Todokoro, and T. Komoda, 1979, J. Electron Microsc. **28**, 1.
Tonomura, A., T. Matsuda, T. Kawasaki, J. Endo, and N. Osakabe, 1985, Phys. Rev. Lett. **54**, 60.
Tonomura, A., T. Matsuda, R. Suzuki, A. Fukuhara, N. Osakabe, H. Umezaki, J. Endo, K. Shinagawa, Y. Sugita, and H. Fujiwara, 1982a, Phys. Rev. Lett. **48**, 1443.
Tonomura, A., T. Matsuda, H. Tanabe, N. Osakabe, J. Endo, A. Fukuhara, K. Shinagawa, and H. Fujiwara, 1982b, Phys. Rev. B **25**, 6799.
Tonomura, A., N. Osakabe, T. Matsuda, T. Kawasaki, J. Endo, S. Yano, and H. Yamada, 1986, Phys. Rev. Lett. **56**, 792.
Tonomura, A., H. Umezaki, T. Matsuda, N. Osakabe, J. Endo, and Y. Sugita, 1984, in *Proceedings of International Symposium on Foundations of Quantum Mechanics, 1983* (Physical So-

ciety of Japan, Tokyo), p. 20.
Wade, R. H., 1980, in *Computer Processing of Electron Microscope Images,* edited by P. W. Hawkes (Springer, Berlin), p. 223.
Wahl, H., 1970, Optik **30**, 508.
Wahl, H., and B. Lau, 1979, Optik **54**, 27.
Walker, I. R., 1986, Phys. Rev. B **33**, 5028.
Weingärtner, I., W. Mirandé, and E. Menzel, 1969, Optik **30**, 318.
Wohlleben, D., 1966, Phys. Lett. **22**, 564.
Worster, J., 1969, J. Phys. D **2**, 457.
Wu, T. T., and C. N. Yang, 1975, Phys. Rev. D **12**, 3845.
Yoshida, K., T. Okuwaki, N. Osakabe, H. Tanabe, Y. Horiuchi, T. Matsuda, K. Shinagawa, A. Tonomura, and H. Fujiwara, 1983, IEEE Trans. Mag. **MAG-19**, 1600.
Zeitler, E., 1979, in *Proceedings of the 37th Electron Microscopy Society of America Meeting,* edited by G. W. Bailey (Claitor, Baton Rouge, Louisiana), p. 376.

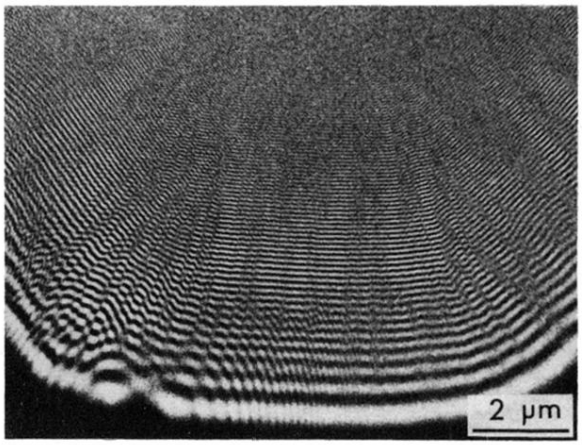

(b)

FIG. 16. Formation of Fresnel fringes, i.e., greatly defocused image of a screen edge: (a) schematic; (b) Fresnel fringes.

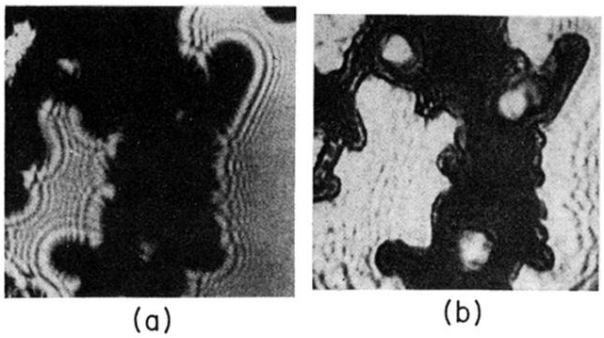

FIG. 17. Image reconstruction of zinc-oxide crystals (Haine and Mulvey, 1952): (a) electron hologram; (b) reconstructed image. An optical image was reconstructed from an in-line electron hologram for the first time, although the image was disturbed by Fresnel fringes that were produced from its conjugate image.

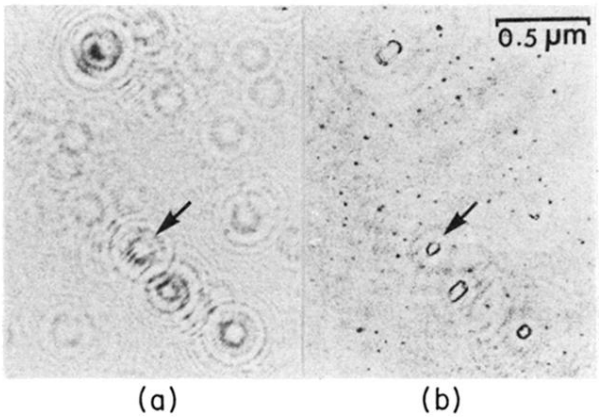

FIG. 19. Image reconstruction of fine gold particles (Tonomura, Fukuhara, Watanabe, and Komoda, 1968): (a) electron hologram; (b) reconstructed image. A clear-cut image was reconstructed free from the disturbances due to the conjugate image, since Fraunhofer holography was adopted.

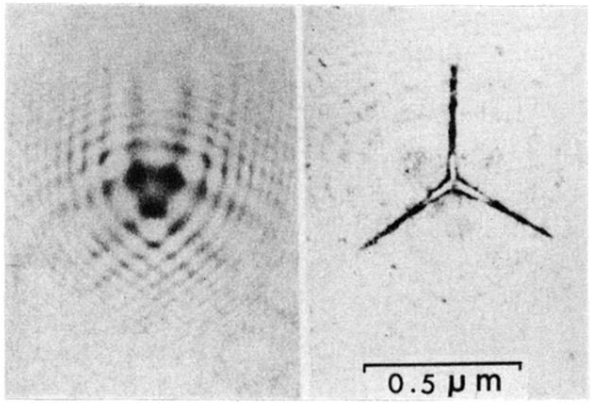

FIG. 20. Image reconstruction of zinc-oxide crystal (Tonomura, Fukuhara, Watanabe, and Komoda, 1968): (a) electron hologram; (b) reconstructed image. Although the size of the whole crystal is too large to satisy the Fraunhofer condition, the needles of the crystal are thin enough to be reconstructed without the conjugate image disturbances.

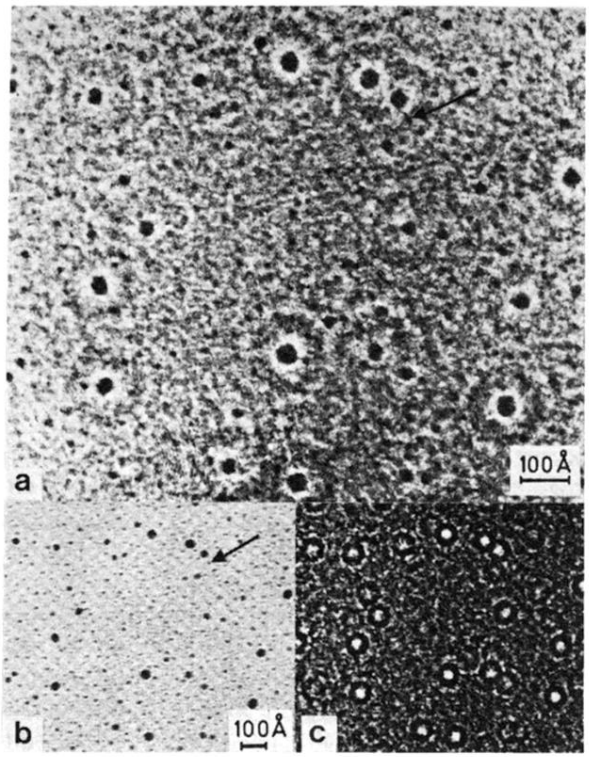

FIG. 21. Image reconstruction of fine gold particles (Munch, 1975): (a) reconstructed image; (b) electron micrograph; (c) electron hologram. An image resolution of 10 Å could be obtained by using both a field-emission electron beam and fine-particle specimens.

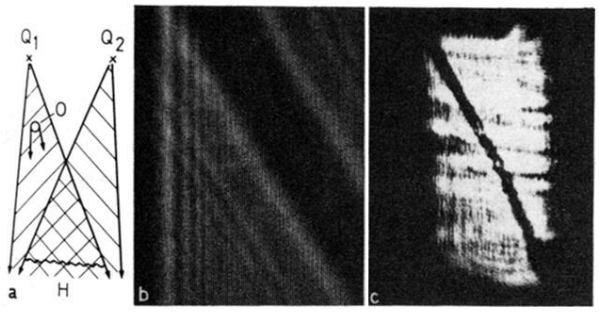

FIG. 22. Image reconstruction of thin tungsten filament (Möllenstedt and Wahl, 1968): (a) schematic for hologram formation; (b) electron hologram; (c) reconstructed image. An optical image was reconstructed from an off-axis one-dimensional electron hologram for the first time.

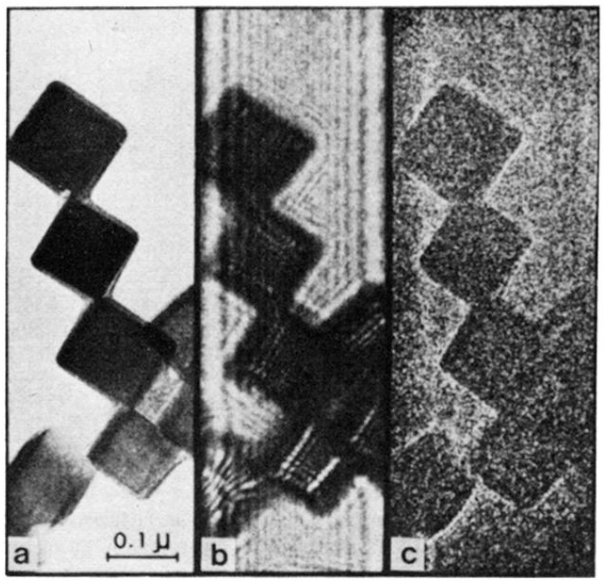

FIG. 23. Image reconstruction of magnesium-oxide particles (Tomita, Matsuda, and Komoda, 1970): (a) electron micrograph; (b) electron hologram; (c) reconstructed image. An optical image was reconstructed from an off-axis Fresnel hologram.

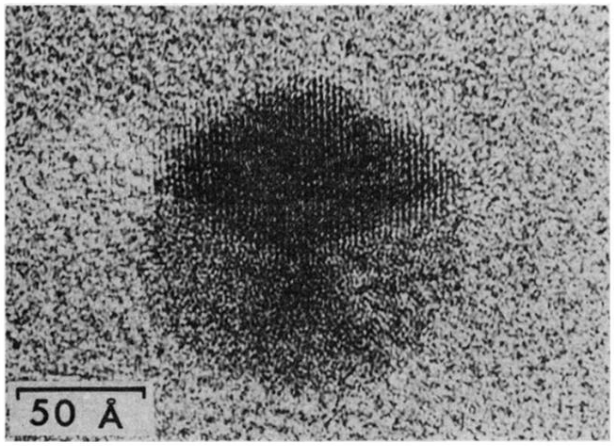

FIG. 24. Reconstructed lattice fringes in a fine gold particle (Tonomura, Matsuda, and Endo, 1979). The lattice resolution of reconstructed images was improved up to 1.2 Å by using a field-emission electron beam; even Bragg-reflected electron beams could be optically reconstructed.

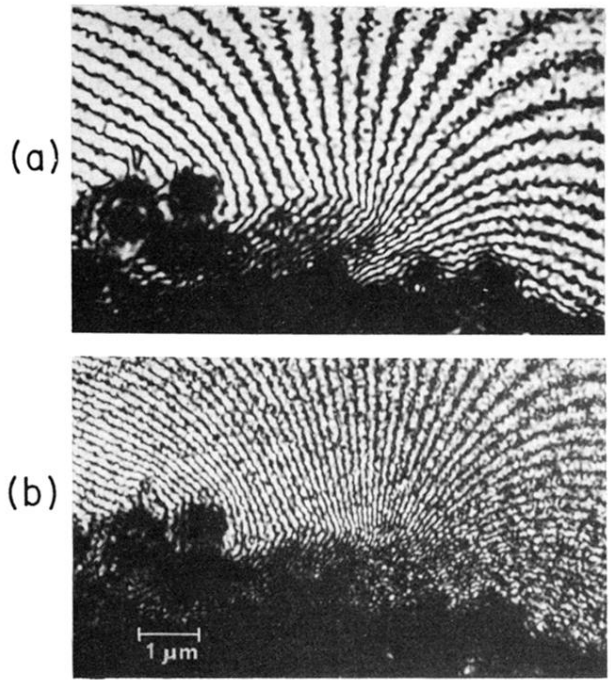

FIG. 32. Equipotential lines near p-n junction observed by electron interferometry (Frabboni, Matteucci, and Pozzi, 1985): (a) reverse bias = 4 V; (b) reverse bias = 8 V. Equipotential lines are directly observed as contour fringes.

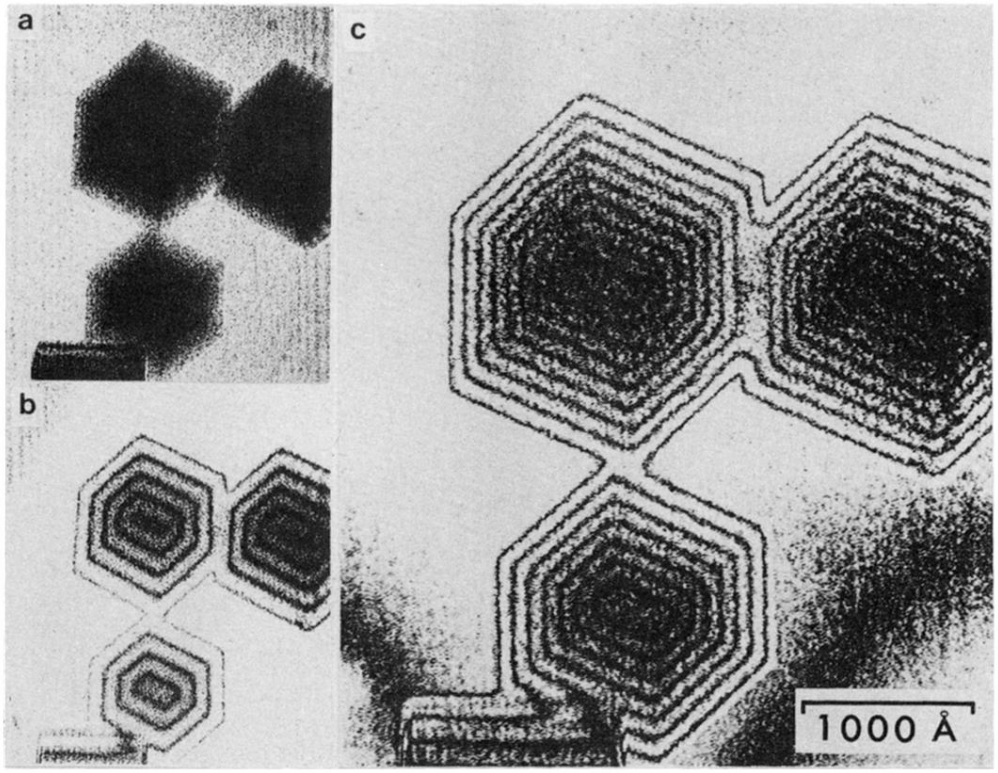

FIG. 33. Interference micrographs of magnesium-oxide particles: (a) reconstructed image; (b) interference micrograph; (c) two-times amplified interference micrograph. Although only the particle outlines can be seen in reconstructed image (a), the thickness distribution can also be observed in interference micrograph (b). Phase-amplified micrograph (c) reveals more detail thickness distribution.

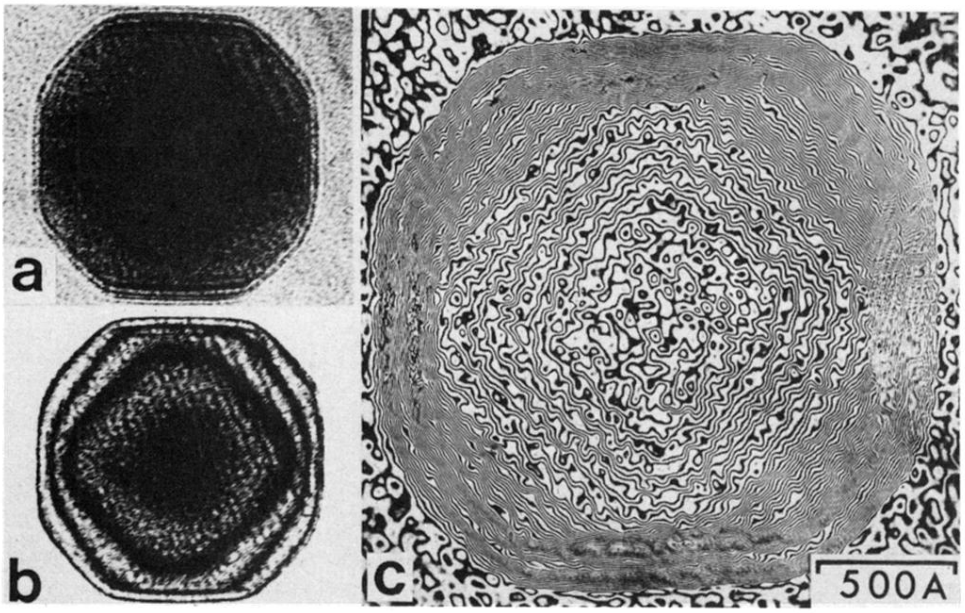

FIG. 35. Interference micrographs of a fine beryllium particle (Endo *et al.*, 1984): (a) reconstructed image; (b) interference micrograph; (c) 32-times amplified interference micrograph. Phase distribution was amplified 32 times, and a thickness contour map in units of only 13 Å was obtained.

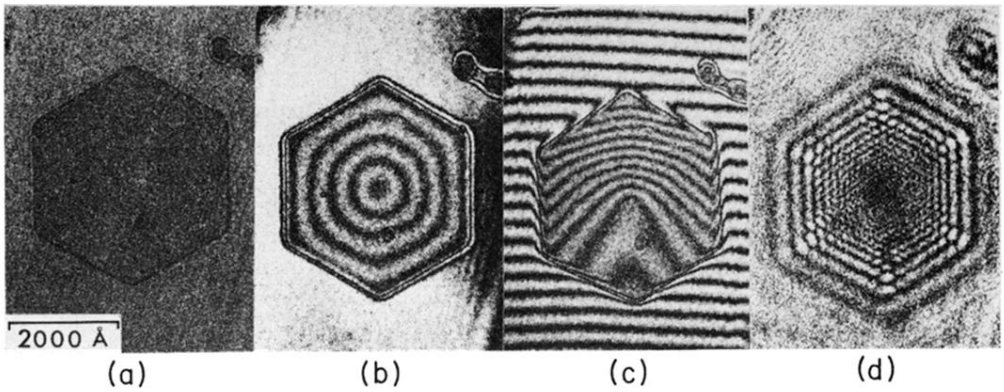

FIG. 38. Interference micrographs of a hexagonal fine cobalt particle: (a) reconstructed image; (b) two-times amplified contour map; (c) two-times amplified interferogram; (d) Lorentz micrograph. No contrast can be observed in reconstructed image (a), while in contour map (b) in-plane magnetic lines of force are displayed as contour fringes. The direction of magnetic line can be determined from interferogram (c) to be clockwise. Lorentz micrograph (d) can also be obtained optically from the same hologram, from which it is difficult to determine the magnetic domain structure.

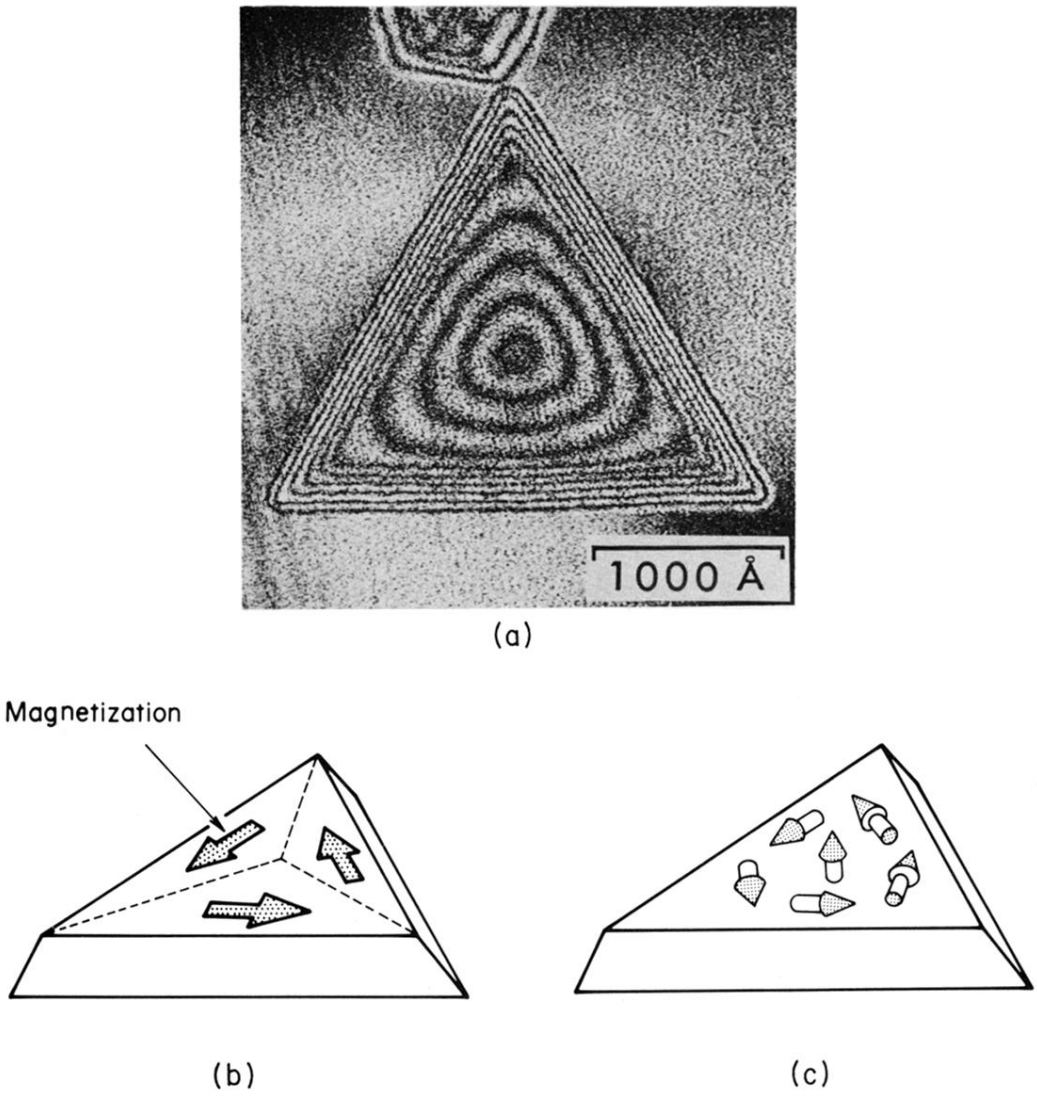

FIG. 39. Interference micrograph of triangular cobalt fine particle (Tonomura, Matsuda, Endo, Arii, and Mihama, 1980): (a) two-times amplified interference micrograph; (b) domain structure; (c) magnetization configuration near the particle center. The peripheral contour fringes in interference micrograph (a) indicate the thickness contour lines, and the inner fringes indicate magnetic lines of force. The detailed examination of the wave front clarified that the magnetization stands up in the central region of the particle 150 Å in radius.

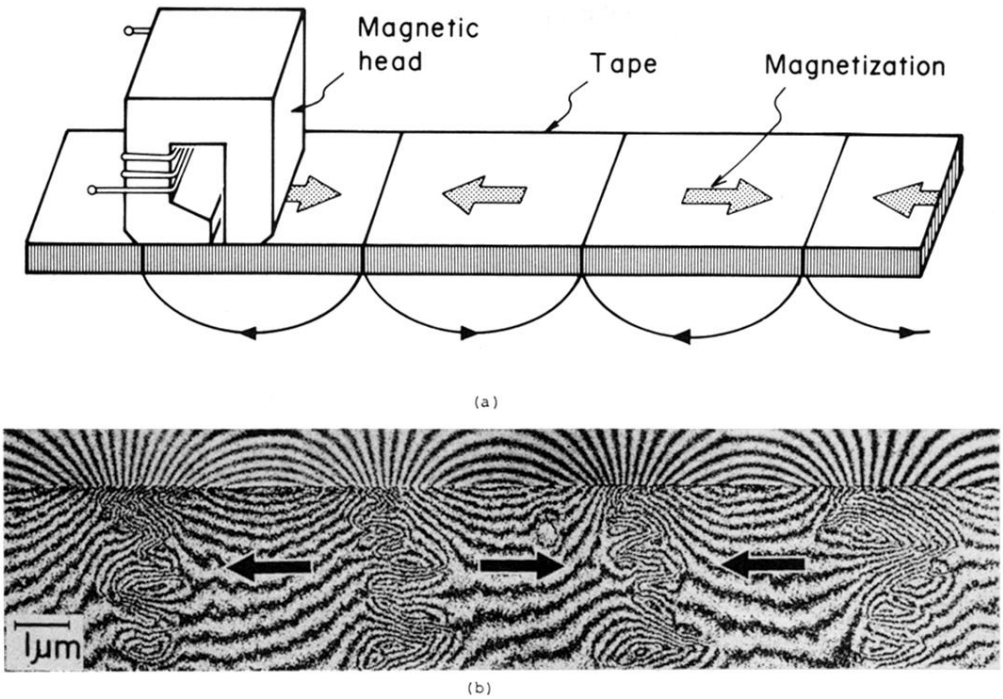

FIG. 41. Recorded magnetization pattern in cobalt magnetic tape: (a) schematic of recording method; (b) two-times amplified interference micrograph.

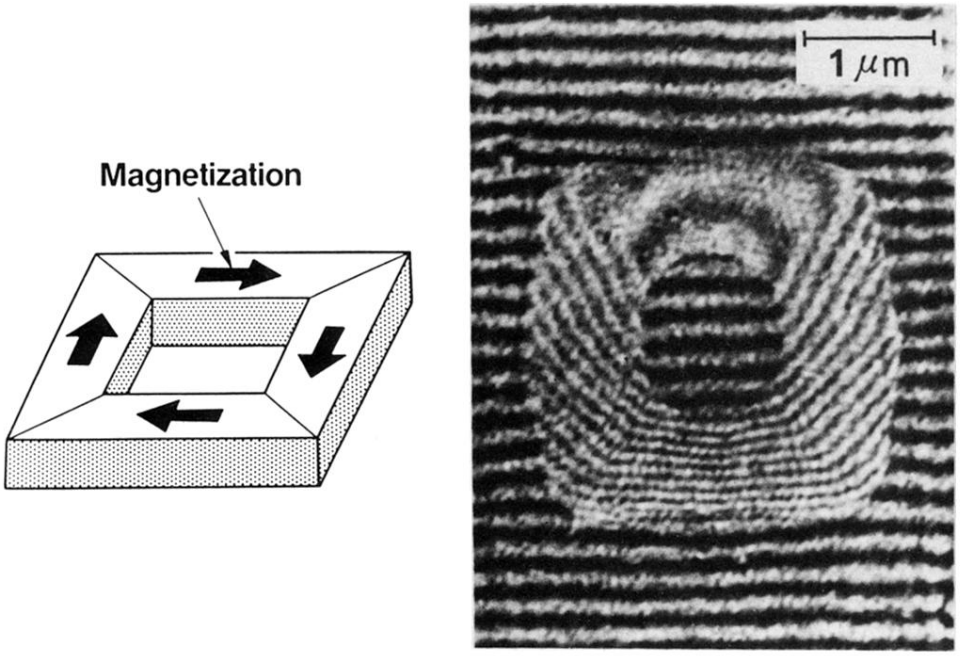

FIG. 45. Experiment to confirm the AB effect (Tonomura *et al.*, 1982a) (a) schematic of toroidal magnet; (b) interferogram. Instead of a solenoid, a ferromagnet with toroidal geometry was employed for the experiment to remove fringing fields. The resultant interferogram (b) indicates that a phase shift of six wavelengths exists between two beams passing through spaces inside the hole and outside the toroid.

FIG. 46. Two-times amplified interference micrograph of toroidal magnet. Since contour fringes indicate magnetic flux in $h/2e$ units, only $\frac{1}{15}$ of the total flux, i.e., a flux of $h/2e$ is leaking outside the toroidal, which is too small to explain the observed phase shift in Fig. 45(b).

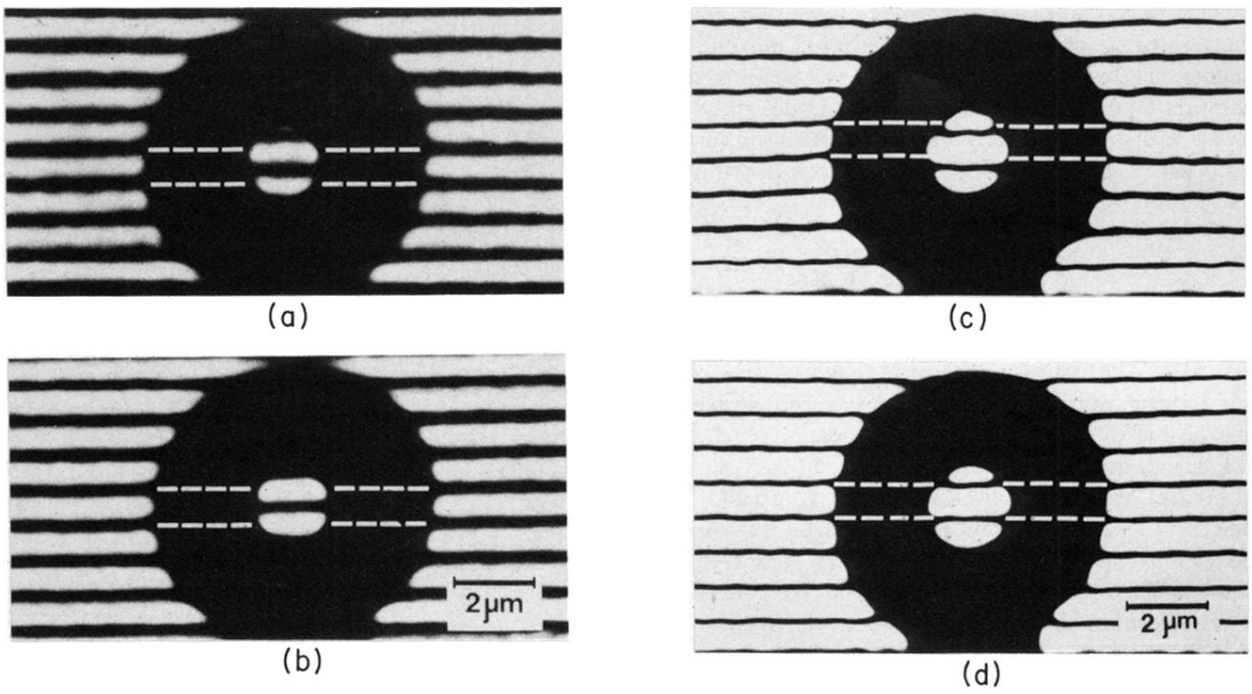

FIG. 48. Interferograms showing phase distribution inside the hole and outside the toroid: (a) interferogram at $T=15$ K; (b) interferogram at $T=4.5$ K; (c) two-times amplified interferogram at $T=15$ K; (d) two-times amplified interferogram at $T=4.5$ K. Interference fringes were displaced by 0.4 fringe spacing between the inside of the hole and the outside of the toroid at 15 K (a). The fringe displacement suddenly changed to just half a spacing (b) when the specimen temperature crossed the critical temperature 9.2 K. This change can be seen clearly in phase-amplified interferograms (c) and (d).